

# Observed Land Impacts on Clouds, Water Vapor, and Rainfall at Continental Scales

MENGLIN JIN,<sup>1</sup> AND MICHAEL D. KING<sup>2</sup>

Short title: Land Impacts at Continental Scales

*Journal of Climate*

(Manuscript submitted September 2005)

---

<sup>1</sup> Earth-Sun Exploration Division, NASA Goddard Space Flight Center; Department of Atmospheric and Oceanic Science, University of Maryland, College Park

<sup>2</sup> Earth-Sun Exploration Division, NASA Goddard Space Flight Center, Greenbelt, Maryland.

## ABSTRACT

How do the continents affect large-scale hydrological cycles? How important can one continent be to the climate system? To address these questions, five years of National Aeronautics and Space Administration (NASA) Terra Moderate Resolution Imaging Spectroradiometer (MODIS) observations, Tropical Rainfall Measuring Mission (TRMM) observations, and the Global Precipitation Climatology Project (GPCP) global precipitation analysis, were used to assess the land impacts on clouds, rainfall, and water vapor at continental scales. At these scales, Empirical Orthogonal Function (EOF) and continentally averaged analyses illustrate that continents as integrated regions enhance the seasonality of atmospheric and surface hydrological parameters. Specifically, the continents of Eurasia and North America enhance the seasonality of cloud optical thickness, cirrus fraction, rainfall, and water vapor. Over land, both liquid water and ice cloud effective radii are smaller than over oceans, primarily because land has more aerosol particles. In addition, different continents have similar impacts on hydrological variables in terms of seasonality, but differ in magnitude. For example, in winter, North America and Eurasia increase cloud optical thickness to 17.5 and 16, respectively, while in summer, Eurasia has much smaller cloud optical thicknesses than North America. Such different land impacts are determined by each continent's geographical condition, land cover, and land use. These new understandings help further address the land-ocean contrasts on global climate, help validate global climate model simulated land-atmosphere interactions, and shed light on interpreting climate change over land.

## 1. Introduction

Land is known to have a larger global surface-warming signal (NRC 2000; Jin and Dickinson 2002; Jin 2004) than oceans. Most likely related to such surface temperature change, the Northern Hemisphere snow cover decreases and annual land precipitation increases at mid- and high latitudes, corresponding to an increase of total cloud cover and water vapor (IPCC 2001, p. 30, and references therein). These observations imply that land affects and responds to global climate change differently than oceans. With use of recently available satellite observations, this study examines the land impacts on clouds, water vapor, and rainfall, with a special focus on the continental scale.

Studying land impacts at continental scales is essential, since land-ocean contrasts on surface temperature partly determine surface circulation (Rasmusson et al. 1993), which in turn modifies the atmospheric 3-cell circulation and consequently affects the displacement of large-scale clouds and rainfall systems (Bjerknes 1966; Wallace and Patton 1970; Wallace and Hobbs 1977; Lau 1982; Holton 2004). Because of its lower heat capacity than water, land warms up more rapidly during summer through radiative heating than does the surrounding ocean (Chen 2003). This results in a secondary circulation with landward wind at lower altitude and oceanward wind at higher altitude, a maintenance mechanism of the summer monsoon system (Wallace and Hobbs 1977, Chen 2003). Many studies of land impacts on clouds and rainfall have been at local (e.g., urban) or regional (e.g., deforestation) scales. For example, land use and land cover prove to be one of the dominant forces for local and regional climate change (Henderson-Sellers et al. 1988; Shuttleworth et al. 1991; Sud et al. 1996). Studies show that urbanization modifies nearby rainfall intensity, duration, and peak time (Shepherd and Burian 2003) and changes surface temperature, aerosol,

and cloud features (Landsberg 1970; Oke 1982; Jin et al. 2005a,b). Nevertheless, the integrated impacts of land as a continent, which should more significantly affect global energy and water cycles, are under-studied (Lawford et al. 2005). How land differs from ocean on continental scales is an important question that needs to be addressed in order to fully understand land-ocean-atmosphere interactions.

Covering about 70% of the Earth's surface, clouds reflect shortwave radiation and absorb and emit longwave radiation (Hartmann et al. 1992). Therefore, the role of clouds in the Earth's climate system cannot be overestimated (Arakawa 2004). ISCCP data for 1982-1996 showed that 64% of the globe is covered by clouds, while only 54% of the Northern Hemisphere land, 53% of the Southern Hemisphere land, 66% of the Northern Hemisphere ocean, and 70% of the Southern Hemisphere ocean are covered by clouds. A slight difference in daytime and nighttime cloudiness was also detected (Hahn et al. 1994). With the advent of the multispectral and high spatial resolution MODIS instrument on Terra and Aqua, these newer observations show that the globe is generally 68-70% covered by clouds, depending on satellite (Platnick, personal communication, 2005). Unfortunately, clouds are the major uncertainty in model response to climate forcing (Cess et al. 1989). Accurate measurements of cloud properties including cloud optical thickness, cloud particle size, cloud cover, and cloud spatial, vertical, and temporal distribution are highly desired.

Although a tremendous number of studies have been done on clouds and cloud feedback in the climate system (see reviews of Wielicki et al. 1995; Soden et al. 2004; Stephens 2005), analyzing new observations from a new viewpoint is still needed. The new observations used here are the recently available National Aeronautics and Space Administration (NASA) Terra Moderate Resolution Imaging Spectroradiometer (MODIS) observations, that provide cloud optical and

microphysical properties during the daytime and cloud physical properties and water vapor information both day and night (King et al. 2003, Platnick et al. 2003). The four times per day measurements obtained from Aqua and Terra reveal diurnal and semi-diurnal information, a piece of information critical for surface energy budget and model validation (Dai et al. 1999, Jin 2000, Wood et al. 2002, Tian et al. 2004). In addition, effective radius is one of the most critical cloud microphysical variables that is needed for cloud parameterization in climate models (McFarquhar et al. 2003). MODIS-provided effective radius for liquid water and ice clouds, for the first time, makes it possible to assess the global distribution of this variable and to examine the contrast between land and ocean.

MODIS observations, like any other observations, have uncertainty. Nevertheless, limited to current remote sensing technology and theoretical understanding of the complex cloud and water vapor retrievals, certain uncertainties have been reported (Platnick et al. 2003). We suggest, nevertheless, to most effectively take advantage of these data sets, more attention needs to be put on spatial and temporal patterns and differences rather than on absolute values over one given pixel at one particular time. More intercomparisons with other datasets such as ISCCP and CERES are ongoing, but reporting those results is beyond the scope of this paper.

Since clouds, water vapor, and rainfall are closely related to each other, to study land continental impacts on the hydrological cycle, these three variables shall be best examined simultaneously. Based on such philosophy, this paper makes extensive use of MODIS observations, combined with the Tropical Rainfall Measuring Mission (TRMM) and Global Precipitation Climatology Project (GPCP) global precipitation analysis, to examine monthly cloud, water vapor, and rainfall seasonal and interannual variations for providing a better understanding of land continental impacts on atmospheric hydrological variables. In

particular, we try to address the following questions:

- (a) What are the observed geographical distributions of water vapor, rainfall, cirrus fraction, cloud optical thickness, and effective cloud particle size?
- (b) What are the continental average values for these variables over given regions and seasons? What are the maxima and minima of these variables on continental averages?

Section 2 describes the datasets and background information used for our analysis of water vapor, clouds, cirrus fraction, and rainfall retrieval. Section 3 discusses results, and is followed by a section of final discussion and remarks (Section 4).

## 2. Data

Five years (April 2000 to April 2005) of cloud properties, including cloud optical thickness<sup>3</sup>, cirrus fraction, water vapor, and effective radius for liquid water and ice clouds measured by MODIS (Gao et al. 2002; King et al. 2003; Platnick et al. 2003; Seaman et al. 2003) were used in this study. MODIS uses infrared bands to determine cloud physical properties related to cloud top pressure and temperature, and visible and near-infrared bands to determine cloud optical and microphysical properties. Nakajima and King (1990) showed that the reflection function of clouds at a non-absorbing band in the visible wavelength region (e.g., 0.66  $\mu\text{m}$ ) is primarily a function of cloud optical thickness, whereas the reflection function at a liquid water (or ice) absorbing channel in the near-infrared (i.e., 1.6 or 2.1  $\mu\text{m}$ ) is a function of cloud particle size. This algorithm, together with ex-

---

<sup>3</sup> Cloud optical thickness is a dimensionless integral of the extinction coefficient along a vertical path through the cloud. It is determined by liquid water path and effective radius. Liquid water path is the weight of liquid water droplets in the atmosphere above a unit surface area on the earth ( $\text{g m}^{-2}$ ). Effective radius is the ratio of volume to area of cloud drops or ice crystals integrated over the cloud particle size distribution.

tensions to distinguish between liquid water and ice clouds and to consider reflection by various underlying surfaces, including snow and sea ice (King et al. 2004), has been incorporated into the operational MODIS retrieval algorithm. MODIS gives cloud droplet size ( $r_e$ ) in two thermodynamic phases, viz., cloud effective droplet size for liquid water ( $r_{ew}$ ) and for ice ( $r_{ei}$ ). The cloud liquid (and ice) water path is calculated from the product of the retrieved cloud optical thickness ( $\tau_c$ ) and effective radius  $r_e$ , after allowing for the different densities of liquid water and ice particles.

The MODIS-derived atmospheric profiles product (King et al. 2003; Seemann et al. 2003) is produced using 12 infrared bands with wavelengths between 4.47 and 14.24  $\mu\text{m}$ , and includes atmospheric profiles of atmospheric temperature and moisture layers, total column ozone, and total precipitable water. Of particular interest to this study is the water vapor in the total atmospheric column, which has important applications to climate studies.

Corresponding monthly mean rainfall measurements from TRMM satellite (Simpson et al. 1988) and GPCP microwave and geosynchronous satellite analysis (Adler et al. 2003) are used to show the different features of surface precipitation over different continents. Specifically, we analyzed land rain gauge data originally provided by the Global Precipitation Climatology Center (GPCC). The spatial resolution of the satellite precipitation data is  $1^\circ \times 1^\circ$  for TRMM and  $2.5^\circ \times 2.5^\circ$  for GPCP.

### 3. Results

#### *a. Global distribution and continental average*

Cloud optical thickness ( $\tau_c$ ) varies across the globe and has evident seasonality (Figure 1). The optically thickest clouds are present over land rather than over ocean, in particular over western Eurasia, east Asia, and southeastern South

America. The cloud optical thickness over these areas is about 30 all year around. The minimum  $\tau_c$  ( $< 10$ ) occurs over ocean regions related to subtropical subsidence. In addition, other regions, including eastern North America, have large  $\tau_c$  up to 30 during winter months (cf. November–February). No satellite observations are available for Greenland during winter months because the satellite algorithm requires reflected sunlight, but large  $\tau_c$  values are observed in September, October, February, and March.

Globally averaged cloud optical thickness over land is larger than that of ocean, with values ranging from 12–15 for land but only 11–13 for ocean (Figure 2a). Larger  $\tau_c$  corresponds to more reflection or scattering of shortwave downward solar radiation, and results in less surface insolation. In addition, land has more evident seasonality than ocean does. The peak  $\tau_c$  of land occurs in October 2000–2002 and in November 2003. Continental-wide averaged  $\tau_c$  for North America, Eurasia, and the whole Northern Hemisphere (poleward of  $70^\circ\text{N}$  is not included) is shown in Figure 2b, further proving that land has larger  $\tau_c$  than ocean. Furthermore, each continent has distinct seasonality and magnitude. For example, North America has higher  $\tau_c$  than Eurasia. Both Eurasia and North America have peak  $\tau_c$  during winter seasons (November–February), while North America has its minimum  $\tau_c$  in March and Eurasia has its minimum in July or August. Finally, Eurasia has relatively noisier seasonal and interannual variations than North America.

Clouds result from large-scale dynamics as well as local convection. Therefore, analyses over different regions serve to illustrate what region, with corresponding dynamical or thermodynamical systems, contributes most to the continentally-averaged seasonality observed in Figure 2. Figure 3 shows that zonally-averaged  $\tau_c$  over  $0^\circ$ – $10^\circ\text{N}$  and  $30^\circ$ – $40^\circ\text{N}$  have the largest differences among land and ocean surfaces. For  $50^\circ$ – $60^\circ\text{N}$  latitude zone, land  $\tau_c$  are larger than the cloud



optical thickness of ocean regions. Although all zonal bands have distinct seasonality, they are different in many details. First, the amplitude of seasonality (peaks minus minimum values) is different. The smallest seasonality occurs in 20°-30°N and the largest seasonality in 50°-60°N. Second, low latitudes (0°-10°N, 10°-20°N) have peak values of  $\tau_c$  in July and minimum values during January-March, but high latitudes (40°-50°N, 50°-60°N) have peak  $\tau_c$  occurring in January. In addition, high latitudes have much larger  $\tau_c$  than low latitudes do. For example, 50°-60°N has the minimum  $\tau_c$  of 14 and a maximum  $\tau_c$  of 15 in January. Over the Northern Hemisphere, the lowest zonal  $\tau_c$  occurs in 10°-20°N during the wintertime, with a value only 5.5 for both land and ocean in January 2001, March 2002 and March 2003. These features are determined by the different climate systems in subtropical and mid- and high latitudes.

Figure 4 shows the geographical distributions of cloud effective radius for liquid water clouds ( $r_{ew}$ ) and ice clouds ( $r_{ei}$ ), averaged from April 2000 to July 2003. The overall pattern between  $r_{ew}$  (Figure 4a) and  $\tau_c$  are very similar. For liquid water clouds, the maximum drop size occurs over the western tropical Pacific warm pool region, where large evaporation associated with large sea surface temperature exists. Both land and ocean have large  $r_{ew}$  variations with the minimum as low as 5  $\mu\text{m}$  and the maximum monthly mean up to  $\sim 22 \mu\text{m}$  in the tropical oceanic regions. In general, oceans have larger values of  $r_{ew}$  and relatively moderate variations, whereas land surfaces have smaller values of  $r_{ew}$  because land regions have more aerosols from dust, biomass burning, or urbanization that serve as cloud condensation nuclei (CCN).

In contrast, for ice clouds, the particle size has relatively small differences between land and ocean regions, except over snow and sea ice surfaces such as the Antarctic continent and high northern latitudes (Figure 4b).

High-resolution MODIS measurements illustrate the fine cloud spatial struc-

ture at 1 km. In order to make full use of such observations, two kinds of statistics are provided: (i) the averaged variable scaled up from 1 km to the model grid box and averaged over time (in our case, monthly mean data at  $1^\circ \times 1^\circ$ ), and (ii) the standard deviation of the variable over the same grid scale (cf. King et al. 2003). Standard deviation represents the spread of the data about the mean distribution (Wilks 1995). This variable also reveals the heterogeneity of the physical variable. From the standard deviation, the land-sea differences are especially evident. For example, Figure 5 shows the standard deviation of cloud optical thickness for July 2004, where Figure 5a pertains to liquid water clouds and Figure 5b to ice clouds. These results show that the largest values of the standard deviation of  $\tau_c$  occur over land for liquid water clouds ( $>15$ ), with the maxima of 30 over southern South America. Desert regions have small standard deviations in  $\tau_c$  in part because of the low overall occurrence of cloud and the generally small optical thickness of these clouds when they occur. Similarly, the standard deviation of ice clouds is even higher over land than liquid water clouds, with values above 15 over 67% of all land surfaces. This means that ice clouds have much more temporal heterogeneity. Oceanic ice clouds have high temporal heterogeneity as well, especially in the Intertropical Convergence Zone.

A closer look at the continental scale (Figure 6) further confirms that land has smaller  $r_e$  than ocean, especially for liquid water clouds, and has larger seasonal variations for both liquid water and ice clouds. Specifically,  $r_{ew}$  varies from 11 to  $14.5 \mu\text{m}$  for the North American continent (13 to  $14.5 \mu\text{m}$  for Eurasia) but much more moderately for the Northern Hemisphere that includes both land and ocean from 13.5 to  $15.2 \mu\text{m}$  (Figure 6a). Furthermore, North America has a larger interannual  $r_{ew}$  variation than Eurasia. By comparison, the differences in  $r_{ei}$  between the three regions are much less distinct, with  $r_{ei}$  being the largest in January and February and the smallest in July, in stark contrast to  $r_{ew}$ , which is larg-

est in July and the smallest in January and February. In addition,  $r_{ei}$  ranges from 25-29  $\mu\text{m}$  continentally (Figure 6b), which is larger than the hemispheric average, suggesting that land increases the spread of  $r_{ei}$ .

Similar to  $\tau_c$ , cirrus fraction varies across the globe and has evident seasonality (Figure 7), with maximum occurring over the Tibetan plateau region. Low values are observed over subtropical subsidence and North Pole regions where low humidity and low temperature are present. A maximum of  $\sim 0.8$  occurs over the Antarctic continent in the Spring and Summer months (September–February), and Greenland and North America in March and April related to the transition time. The Andes has high cirrus fraction all year around. In general, land has higher cirrus fraction than ocean. For example, Asia has a cirrus fraction around 0.5 in all months, while most ocean regions have  $<0.3$  in the tropics and subtropics.

At continental scales, land enhances the amplitude of the annual cycle of cirrus fraction by about 50% (cf. Figure 8), since the Northern Hemisphere ranges from 0.35-0.45, but North America ranges from 0.35-0.60 and Eurasia from 0.27-0.5. Specifically, the seasonality of cirrus fraction is clear for both continents with minima in July and August and maxima in March and April.

Globally, land has persistently lower water vapor amounts than ocean regions (Figure 9a). Water vapor ranges from 2.0 to 2.7 cm for global ocean and from 1.3 to 2.4 cm for global land. This may be because oceans have adequate supplies of liquid water at the surface and thus should have maximum evaporation. Nevertheless, water vapor here is column integrated precipitable water, which is determined by surface as well as atmosphere temperatures, dynamics, and surface sources of water (Randel et al. 1996). In addition, continents can differ from one other in their water vapor content (Figure 9b). Eurasia has nearly the same water vapor content as North America. In July, both continents hold

more water vapor than they do in January. The different relationship of land and ocean water vapor between Figures 9a and 9b, namely, globally land has less water vapor than oceans but for specific continents (Eurasia and North America) land has lower amounts of water vapor than the global mean land. This suggests that other continents may be much moister and thus enhance the land-averaged water vapor column amount.

To examine all continents, Figure 10a shows the MODIS-derived global distribution of column water vapor, which varies dramatically over land and ocean. In general, because water vapor is a function of surface temperature, zonal decreases from the moist tropics to the drier Polar Regions are evident. Equatorial regions have higher water vapor because of high surface temperature and adequate water supplies of water from the surface. Greenland, the Tibetan plateau, and the Andes Mountains have minimum water vapor because of low temperature in the atmosphere that can thus hold little water vapor. The Saharan Desert and neighboring Arabian Peninsula have small water vapor content because little water can be transported and held in these hot desert regions. Evident seasonal changes of water vapor over the globe are observed in Figures 10a and 10b. In January, land over the Northern Hemisphere has uniformly smaller water vapor ( $\sim 0.5$  cm) because of the cold land and atmospheric temperature at that time of year. In addition, the maximum centers of water vapor have shifted south in January, which is related to the seasonal variation of solar illumination.

A study of land impact on the atmospheric hydrological cycle would not be complete without examining rainfall, as water vapor, clouds, and rainfall are closely related to one other. Figure 11 shows two monthly mean rainfall accumulation images for January and July, respectively. Ocean regions generally have larger rainfall than land regions in tropical and subtropical areas, but such differences are further complicated by land cover evapotranspiration. For exam-

ple, Amazonian forests have significantly more accumulated rainfall than nearby oceans because of the strong evapotranspiration and local convective activity.

As was the case for water vapor and clouds, evident seasonal variation of rainfall can be observed for certain regions (Figure 11b). Further analysis of zonally-averaged monthly rainfall accumulation from TRMM (Figure 12) shows that  $5^{\circ}\text{N}$  has its maximum rainfall amount in July of up to  $\sim 220$  mm, and such maxima shift to  $5^{\circ}\text{S}$  in January and reduces to  $\sim 160$  mm. Minimum rainfall occurs from  $10^{\circ}$ - $20^{\circ}\text{N}$  and  $10^{\circ}$ - $20^{\circ}\text{S}$ , related to subtropical subsidence, where the monthly mean rainfall is generally  $< 20$  mm.

At continental scales, seasonality of rainfall is significant (Figure 13). In July, both Eurasia and North America have much larger rainfall than they do in January. Nevertheless, North America seems to have its peak in September instead of July as in Eurasia. In addition, both continents differ from each other in terms of absolute values of accumulated rainfall. For example, in January 2001, North America had 40 mm of rainfall while Eurasia had only 20 mm, a 50% decrease in continental average. Such differences must be related to both large-scale dynamics as well as local land cover mechanisms (Jin and Zhang 2002). Note that rainfall for the Northern Hemisphere in Figure 13 is based on GPCP rain gauge station data and is only over land and islands. Therefore, the ocean effects cannot directly be included in this figure. Nevertheless, this figure examines the seasonal variation of rainfall for land surfaces and suggests inter-relationship between rainfall, clouds, and water vapor.

#### *b. Diurnal signal*

Diurnal signal means the physical variable variation during timescales less than one day. One of the important features of EOS Terra and Aqua is the ability to provide data assimilation input on environmental properties derived from the

4-times per day satellite measurements. Terra crosses the equator at 10:30 am and 10:30 pm, with Aqua crossing the equator at 1:30 am and 1:30. Such orbital characteristics permit critical diurnal and semi-diurnal information on clouds and water vapor to be derived. For example, Figure 14c is the differences in column water vapor between Aqua (Figure 14b, 1:30 pm) and Terra (Figure 14a, 10:30 am) measurements during the daytime for July 2004. The largest variation between morning and afternoon (also referred to as the semi-diurnal variation) is most significant over equatorial land, with up to 6 cm of precipitable water difference in west Africa, northwestern South America, and Indochina. In general, the land has more water vapor at 1:30 pm than at 10:30 am, largely as a result of higher surface temperature and stronger horizontal advection due to surface wind diurnal circulation.

*c. EOF Analysis*

An Empirical Orthogonal Function (EOF) approach reveal the underlying patterns in the data that can therefore be linked with physical processes. This approach has proven insightful to decompose multi-year satellite observations into several spatial patterns (so-called principal components) and corresponding time-series. Examples of using EOF analyses on large-volume observations can be found in analyses of land surface skin temperature (Jin et al. 1997), convective clouds and precipitation using ISCCP-B3 data (Vuille and Keimig 2004), surface wind speed (Ludwig et al. 2003), and tropical disturbances (Fraedrich et al. 1997). Readers who need more details information on the EOF approach can refer to the pioneering papers of Lorenz (1956), Kutzbach (1967), Hardy (1977), and Ludwig and Byrd (1980). These EOF studies prove that EOF analysis is very valuable for identifying the most important, independent modes of one variable and its diurnal, seasonal, and interannual variations (Wilks 1995). In this paper, we present

EOF analyses to show the important spatial and temporal modes of clouds and water vapor from MODIS observations.

Figure 15a is the 1<sup>st</sup> principal component (EOF1) of the 5 year MODIS cloud optical thickness. We keep the missing value regions (poleward of 60°N and 60°S) in the figure in order to show the limit of the data set and truthfully reporting how we analyze these data, in case others may wish to reproduce such analysis. Most importantly, EOF1 explains 67.3% of the total variance. Corresponding time series illustrate that EOF1 represents the seasonal variations of cloud optical thickness. Because the absolute value of the EOF spatial pattern is not meaningful, we normalized the global map to the range +1 to -1. The normalized value therefore shows the relative importance of each area, and the sign shows whether the variation of each grid is consistent with others. EOF1 shows the similar phase (positive sign) over east coast and northwest coast of USA, Europe, Southeast China, Australia, southern Africa, and the cerrado of Brazil. Meanwhile, northern South America, Equatorial Africa and the region from 120°E, 40°N toward the northeast of China have negative signs. These patterns of clouds are consistent with monsoon patterns over land (Lau 1982, Zeng et al. 2004). With respect to land vs. sea differences, it is evident that larger values are over continents, namely up to  $\pm 0.8$ , than over oceanic regions at the same latitudes. Therefore, we refer to this pattern as “clouds’ monsoon pattern.”

EOF2 explains 12.6% of the total variance. EOF2 is interesting because it clearly reveals the ITCZ-related pattern: the long, persistent cloud system that crosses the central and eastern Pacific and Atlantic Ocean around 5°-10°N. Accompanying this ITCZ cloud system is the opposite-signed maxima to the south. In the Northern Hemisphere, the northwestern United States has an opposite sign to the middle of US, as does Eurasia. EOF3 explains 6.1% of the total variance. Two features are noticeable: one is the ITCZ-related cloud system and its

accompanying opposite-signed system observed in EOF2. Another is that the whole map is rather noisy, implying that this component may not be physically meaningful.

To remove the dominant seasonal pattern shown in Figure 15a, we conducted EOF analysis for summer months only. Namely, we sampled June, July, and August for the five years (2000-2004) to build one time series, and applied EOF analysis to these summer months. In this case, EOF1 explains 74.5% of the total variance (Figure 16a). Several features are worth emphasizing: one is that the ITCZ-related cloud system and its nearby accompanied climate system has a negative sign along the middle-east Pacific and Atlantic Oceans. The southwest coast of the United States and central India show relatively large signals for this mode. EOF2 explains 13.0% of the total variance. EOF3 only explains 2% of the total variance, suggesting EOF3 may not be important to the total cloud variation.

Corresponding EOF analysis has also been performed on summer total column water vapor, as shown in Figure 17. EOF1 explains 70.1% of the total variance, and EOF2 explains 12.5%. The ITCZ related pattern is very evident along the Equator and northwestern United States.

#### **4. Discussions and Remarks**

This paper provides a prototype application of using MODIS and other observations to better understand land-atmosphere interactions. Analyses of the land impacts on clouds, water vapor, cirrus fraction, and rainfall at continental scales from 2000 to 2005 illustrate that land enhances the seasonality of these variables, namely, land enhances the seasonal variation of cloud optical thickness and microphysical properties, column water vapor, and rainfall. Furthermore, land decreases the cloud effective radius, especially for liquid water clouds. Dif-



ferent continents have different characteristics, which in turn are related to details of their land cover, geographic location, and nearby oceanic circulation.

Scale is important in studying land impacts and climate change. Global scales and continental scales may have different distinguishing characteristics. For example, the Eurasian and North American continents hold more precipitable water (column water vapor) than oceans in summer because land areas are warmer than the nearby oceans, but in the global mean, the atmosphere over the land has less water vapor than over oceans in large part because land over high latitudes is much colder and hence contains much less water vapor.

Cloud simulation is one of the weakest parts of current GCMs, partly because of the lack of accurate knowledge of cloud dynamics, cloud microphysics, and cloud-aerosol interactions, and partly because of the unrealistic specification on sub-grid cloud features. For example, the NCAR GCM, like many other GCMs, prescribes cloud effective radius of liquid water as  $10\ \mu\text{m}$  over oceans and  $7\text{-}10\ \mu\text{m}$  over land, whereas MODIS observations show obviously spatial and temporal variations with a maximum up to  $20\ \mu\text{m}$  for liquid droplets over tropical ocean (cf. Figure 4). Over land,  $r_{\text{ew}}$  and  $r_{\text{ei}}$  vary with the underlying surface and aerosol properties through cloud-aerosol interactions (cf. Figure 6). Since in the model  $r_e$  is used to calculate other cloud radiative properties (namely, cloud optical thickness, single scattering albedo, asymmetry factor, and cloud effective emissivity), any error in the prescribed  $r_e$  may propagate into the model's cloud properties and may further propagate into surface temperature and rainfall simulations. Therefore, realistic cloud droplet size is very important in model cloud parameterization.

Accurate cloud, water vapor, and rainfall simulations in climate models require knowledge of land-atmosphere interactions, the basic feature that determines the global water and energy transport. Current GCMs need observations

to validate and improve the models. For example, Figure 18 shows the NCEP reanalysis simulated column water vapor, which is evidently different from MODIS observations (cf. Figure 9b) in both the relative pattern and in quantitative values. MODIS shows the peaks and minimums, namely the seasonal variations, for water vapor for Eurasia and North America at continental scale are very identical, but NCEP shows a difference up-to 40% for the two continents (namely 10 vs. 14 Kg/m<sup>2</sup> in Januarys). In addition, MODIS shows land increases the peaks and decreases the minima, but NCEP shows land and ocean having similar peak time and values. This example suggests the importance of using satellite observations to validate and improve GCMs for a possibly better simulation of the climate system.

Unfortunately, a clear gap exists between remote sensing observations and climate model requirements, partly because limited resources hinder in depth analysis of the rich information content that MODIS, TRMM, and other observations contain, and partly because of the mismatch in the remote sensing and modeling communities. One example for the latter is resolution—MODIS can give 1 km spatial resolution observations while model grids are typically about 100 km. How to scale up high-resolution data meaningfully for GCM use is a challenging task. Only collaboration between remote sensing experts and modelers can possibly fill the gap and make more effective use of satellite observations in GCMs.

Although remote sensing data by themselves are extremely valuable, their uncertainty requires special attention in using these data in climate studies or for improving GCMs. Like any other measurements, MODIS observations have reported uncertainties, for example, instantaneous errors of column water vapor over a 1.5 year time period are accurate to an rms error of about 4.1 mm when compared to collocated ground-based microwave radiometer observations (See-

mann et al. 2003), and ice effective radius is accurate to about  $1.5 \mu\text{m}$  for optically thin cirrus clouds when compared to collocated ground-based millimeter cloud radar observations (Mace et al. 2005). It is important for the users to realize that using data to study the patterns and differences, namely, seasonal, diurnal and interannual variations, rather than absolute values, will make the final result less affected by the uncertainty in the observations.

*Acknowledgments.* We thank NASA EOS Interdisciplinary Science for supporting this work. Special thanks go to Dr. Zhong Liu of NASA DAAC for his helpful on-line data analysis and visualization tools for MODIS and TRMM data. NCEP reanalysis data were downloaded from the NOAA-CIRES Climate Diagnostics Center ([www.cdc.noaa.gov/cdc/reanalysis/reanalysis.shtml](http://www.cdc.noaa.gov/cdc/reanalysis/reanalysis.shtml)).

## REFERENCES

- Adler, R. F., G. J. Huffman, A. Chang, R. Ferraro, P. P. Xie, J. Janowiak, B. Rudolf, U. Schneider, S. Curtis, D. Bolvin, A. Gruber, J. Susskind, P. Arkin, and E. Nelkin, 2003: The version 2 Global Precipitation Climatology Project (GPCP) monthly precipitation analysis (1979 present). *J. Hydrometeor.*, **4**, 1147–1167.
- Arakawa, A., 2004: The cumulus parameterization problem: Past, present, and future. *J. Climate*, **17**, 2493–2525.
- Bjerknes, J., 1966: A possible response of atmospheric Hadley circulation to equatorial anomalies of ocean temperature. *Tellus*, **18**, 820–829.
- Cess, R. D., G. L. Potter, J. P. Blanchet, G. Boer, S. J. Ghan, J. T. Kiehl, X. Z. Liang, J. F. B. Mitchell, J. J. Morcrette, D. A. Randall, M. R. Riches, E. Roeckner, U. Schlese, A. Slingo, K. E. Taylor, W. M. Washington, R. T. Wetherald and I. Yagai, 1989: Intercomparison and interpretation of cloud-climate feedback as produced by fourteen atmospheric general circulation models. *Science*, **245**, 513–516.
- Chen, T. C., 2003: Maintenance of summer monsoon circulation: A planetary-scale perspective. *J. Climate*, **16**, 2022–2037.
- Dai, A., K. E. Trenberth, and T. R. Karl, 1999: Effects of clouds, soil moisture, precipitation, and water vapor on diurnal temperature range. *J. Climate*, **12**, 2451–2473.
- Fraedrich, K., J. L. McBride, W. M. Frank, and R. S. Wang, 1997: Extended EOF analysis of tropical disturbances: TOGA COARE. *J. Atmos. Sci.*, **54**, 2363–2372.
- Gao, B. C., P. Yang, W. Han, R. R. Li, and W. J. Wiscombe, 2002: An algorithm using visible and 1.38- $\mu\text{m}$  channels to retrieve cirrus cloud reflectances from aircraft and satellite data. *IEEE Trans. Geosci. Remote Sens.*, **40**, 1659–1668.

- Hahn, C. J., S. G. Warren, and J. London, 1994: *Edited Synoptic Cloud Reports from Ships and Land Stations Over the Globe, 1982-1991*. NDP-026B, Carbon Dioxide Information Analysis Center, Oak Ridge National Laboratory, Oak Ridge, Tennessee.
- Hardy, D. M., 1977: Empirical eigenvector analysis of vector observations. *Geophys. Res. Letters*, **4**, 319–320.
- Hartmann, D. L., M. E. Ockert-Bell, and M. L. Michelsen, 1992: The effect of cloud type on Earth's Energy Balance: Global Analysis. *J. Climate*, **5**, 1281–1304.
- Henderson-Sellers, A., R. E. Dickinson, and M. F. Wilson, 1988: Tropical deforestation—Important processes for climate models. *Climate Change*, **13**, 43–67.
- Holton, J. R., 2004: *Introduction to Dynamic Meteorology, Fourth Edition*. Elsevier Academic Press, 529 pp.
- IPCC, The Intergovernmental Panel on Climate Change, 2001: *Climate Change 2001: The Scientific Basis*. Cambridge University Press, 881 pp.
- Jin, M., 2000: Interpolation of surface radiation temperature measured from polar orbiting satellites to a diurnal cycle. Part 2: Cloudy-pixel treatment. *J. Geophys. Res.*, **105**, 4061–4076.
- \_\_\_\_\_, 2004: Analyzing skin temperature variations from long-term AVHRR. *Bull. Amer. Meteor. Soc.*, **85**, 587–600.
- \_\_\_\_\_, and R. E. Dickinson, 2002: New observational evidence for global warming from satellite data. *Geophys. Res. Lett.*, **29**(10), doi:10.1029/2001GL013833.
- \_\_\_\_\_, R.E. Dickinson, and A. M. Vogelmann, 1997: A comparison of CCM2/BATS skin temperature and surface-air temperature with satellite and surface observations. *J. Climate*, **10**, 1505–1524.
- \_\_\_\_\_, \_\_\_\_\_, and D. L. Zhang, 2005a: The footprint of urban areas on global climate as characterized by MODIS. *J. Climate*, **18**, 1551–1565.
- \_\_\_\_\_, J. M. Shepherd, and M. D. King, 2005b: Urban aerosols and their interaction

- with clouds and rainfall: A case study for New York and Houston. *J. Geophys. Res.*, **110**, D10S20, doi:10.1029/2004JD005081.
- King, M. D., W. P. Menzel, Y. J. Kaufman, D. Tanré, B. C. Gao, S. Platnick, S. A. Ackerman, L. A. Remer, R. Pincus, and P. A. Hubanks, 2003: Cloud and aerosol properties, precipitable water, and profiles of temperature and humidity from MODIS. *IEEE Trans. Geosci. Remote Sens.*, **41**, 442–458.
- \_\_\_\_\_, S. Platnick, P. Yang, G. T. Arnold, M. A. Gray, J. C. Riédi, S. A. Ackerman, and K. N. Liou, 2004: Remote sensing of liquid water and ice cloud optical thickness and effective radius in the arctic: Application of airborne multispectral MAS data. *J. Atmos. Oceanic Technol.*, **21**, 857–875.
- Kutzbach, J. E., 1967: Empirical eigenvectors of sea-level pressure, surface temperature and precipitation complex over North America. *J. Appl. Meteor.*, **6**, 791–802.
- Landsberg, H. E., 1970: Man-made climatic changes. *Science*, **170**, 1265–1274.
- Lau, K. M., 1982: Thermally driven motions in an equatorial  $\beta$ -plane: Hadley and Walker circulations during the winter monsoon. *Mon. Wea. Rev.*, **110**, 336–353.
- Lawford, R. G., R. Stewart, J. Roads, H. J. Isemer, M. Manton, J. Marengo, T. Yasunari, S. Benedict, T. Koike, and S. Williams, 2005: Advancing global- and continental-scale hydrometeorology: Contributions of GEWEX hydrometeorology panel. *Bull. Amer. Meteor. Soc.*, **85**, 1917–1930.
- Lorenz, E. N., 1956: Empirical Orthogonal Functions and Statistical Weather Prediction, Scientific Report 1. Statistical Forecasting Project, Mass. Inst. Technol., Cambridge, Mass., Deference Doc. Center No. 110268, 49 pp.
- Ludwig, F. L., and G. Byrd, 1980: A very efficient method for deriving mass consistent flow fields from wind observations in rough terrain. *Atmos. Environ.*, **14**, 585–587.

- \_\_\_\_\_, J. Horel, and C. D. Whiteman, 2003: Using EOF analysis to identify important surface wind patterns in Mountain Valleys. *J. Appl. Meteor.*, **43**, 969–983.
- Mace, G. G., Y. Zhang, S. Platnick, M. D. King, P. Minnis, and P. Yang, 2005: Evaluation of cirrus cloud properties derived from MODIS data using cloud properties derived from ground-based observations collected at the ARM SGP site. *J. Appl. Meteor.*, **44**, 221–240.
- McFarquhar, G. M., S. Iacobellis and R. C. J. Somerville, 2003: SCM simulations of tropical ice clouds using observationally based parameterizations of microphysics. *J. Climate*, **16**, 1643–1658.
- Nakajima, T., and M. D. King, 1990: Determination of the optical thickness and effective particle radius of clouds from reflected solar radiation measurements, Part I: Theory. *J. Atmos. Sci.*, **47**, 1878–1893.
- NRC, National Research Council, 2000: *Reconciling Observations of Global Temperature Change*. National Academy Press, 85 pp.
- Oke, T. R., 1982: The energetic basis of the urban heat island. *Quart. J. Roy. Meteor. Soc.*, **108**, 1–24.
- Platnick, S., M. D. King, S. A. Ackerman, W. P. Menzel, B. A. Baum, J. C. Riédi, and R. A. Frey, 2003: The MODIS cloud products: Algorithms and examples from Terra. *IEEE Trans. Geosci. Remote Sens.*, **41**, 459–473.
- Randel, D. L., T. H. Vonder Haar, M. A. Ringerud, G. L. Stephens, T. J. Greenwald, and C. L. Combs, 1996: A new global water vapor data set. *Bull. Amer. Meteor. Soc.*, **77**, 1233–1246.
- Rasmusson, E. M., R. E. Dickinson, J. E. Kutzbach, and M. K. Cleveland, 1993: Climatology. *Handbook of Hydrology*, D. R. Maidment, Ed., McGraw-Hill Professional, 2.1–2.43.
- Seemann, S. W., J. Li, W. P. Menzel, and L. E. Gumley, 2003: Operational retrieval of atmospheric temperature, moisture, and ozone from MODIS infrared ra-

- diances. *J. Appl. Meteor.*, **42**, 1072–1091.
- Shepherd, J. M., and S. J. Burian, 2003: Detection of urban-induced rainfall anomalies in a major coastal city. *Earth Interactions*, **7**(4), doi:10.1175/10873562(2003)007.
- Shuttleworth, W. J., J. H. C. Gash, J. M. Roberts, C. A. Nobre, L. C. B. Molion, and M. N. G. Ribeiro, 1991: Post-deforestation Amazonian climate: Anglo-Brazilian research to improve prediction. *J. Hydrol.*, **129**, 71–85.
- Simpson, J., R. F. Adler, and G. R. North, 1988: A proposed Tropical Rainfall Measuring Mission (TRMM) satellite. *Bull. Amer. Meteor. Soc.*, **69**, 278–295.
- Soden, B. J., A. J. Broccoli, and R. S. Hemler, 2004: On the use of cloud forcing to estimate cloud feedback. *J. Climate*, **17**, 3661–3665.
- Stephens, G. L. 2005: Cloud feedbacks in the climate system: A critical review. *J. Climate*, **18**, 237–273.
- Sud, Y. C., G. K. Walker, J. H. Kim, G. Liston, P. J. Sellers, and W. K. M. Lau, 1996: Biogeophysical consequences of a tropical deforestation scenario: AGCM simulation study. *J. Climate*, **9**, 3225–3247.
- Tian, B., B. J. Soden, X. Wu, 2004: Diurnal cycle of convection, clouds, and water vapor in the tropical upper troposphere: Satellite versus a general circulation model. *J. Geophys. Res.*, **109**, doi:10.1029/2003JD004117.
- Vuille, M., and F. Keimig, 2004: Interannual variability of summertime convective cloudiness and precipitation in the central Andes derived from ISCCP-B3 Data. *J. Climate*, **17**, 3334–3348.
- Wallace, J. M., and P. V. Hobbs, 1977: *Atmospheric Sciences: An Introductory Survey*. Academic Press, Inc., 467 pp.
- \_\_\_\_\_, and D. B. Patton, 1970: Diurnal temperature variations—Surface to 25 kilometers. *Mon. Wea. Rev.*, **98**, 548–552.
- Wielicki, B. A., R. D. Cess, M. D. King, D. R. Randall, and E. F. Harrison, 1995:



Mission to Planet Earth: Role of clouds and radiation in climate. *Bull. Amer. Meteor. Soc.*, **76**, 2125–2153.

Wilks, D. S., 1995: *Statistical Methods in the Atmospheric Sciences*. Academic Press, Inc., 464 pp.

Wood, R., C. S. Bretherton, and D. L. Hartmann, 2002: Diurnal cycle of liquid water path over the subtropical and tropical oceans. *Geophys. Res. Lett.*, **29**(23), 2092, doi:10.1029/2002GL015371.

Zeng, X., and E. Lu, 2004: Globally unified monsoon onset and retreat indexes. *J. Climate*, **17**, 2241–2248.

## FIGURE LEGENDS

- Figure 1. Monthly mean cloud optical thickness from April 2000-July 2004.
- Figure 2. Monthly mean cloud optical thickness as a function of time (a) for global land and ocean, and (b) for North America, Eurasia, and the Northern Hemisphere.
- Figure 3. Zonal mean cloud optical thickness as a function of time for land and ocean regimes. In the legend, "Global Land" and "Global Ocean" means zonal averages for land and ocean for the specific latitude bands, respectively.
- Figure 4. Monthly mean cloud effective radius for (a) liquid water clouds and (b) ice clouds from April 2000-July 2004.
- Figure 5. Monthly mean standard deviation of cloud optical thickness for  $1^\circ \times 1^\circ$  grid cells on July 2004 for (a) liquid water clouds and (b) ice clouds.
- Figure 6. Monthly mean cloud effective radius as a function of time for (a) liquid water clouds and (b) ice clouds.
- Figure 7. Monthly mean cirrus fraction from April 2000-July 2004.
- Figure 8. Monthly mean cirrus fraction as a function of time for North America, Eurasia, and the Northern Hemisphere.
- Figure 9. Monthly mean precipitable water as a function of time (a) for global land and ocean, and (b) for North America, Eurasia, and the Northern Hemisphere ocean.
- Figure 10. Monthly mean precipitable water for (a) January 2004 and (b) July 2004.
- Figure 11. Accumulated rainfall measured from TRMM for (a) January 2004 and (b) July 2003.
- Figure 12. Zonally-averaged monthly mean accumulated rainfall from TRMM

observations at 180°W.

Figure 13. Monthly rainfall for the Northern Hemisphere, North America, and Eurasia. Data are based on GPCP analysis.

Figure 14. Diurnal signal of water vapor over land vs. ocean. (a) Terra water vapor observations for July 2004; (b) same as (a) except for Aqua; and (c) the difference between afternoon and morning Aqua minus Terra). Note that the data southward of 15°S is un-retrieval in MODIS water vapor NIR algorithm (Gao et al. 2002).

Figure 15. EOF reanalysis on 5-year (April 2000 – April 2005) monthly Terra/MODIS measurement for cloud optical thickness. (a) is the first principal component (EOF1); (b) is the second principal component (EOF2); and (c) is the third principal component (EOF3). The explained variance for each component is given at the left of each panel. The extremely small values poleward of 60°N and 60°S and the box-outlined regions over Africa are missing values.

Figure 16. As in Figure 15, except for summer clouds.

Figure 17. Results of EOF analysis on 5-year MODIS water vapor for summer time. (a) is EOF1; (b) is EOF2, and (c) EOF3.

Figure 18. NCEP reanalysis simulated precipitable water vapor for North America, Eurasia, and the North Hemisphere.

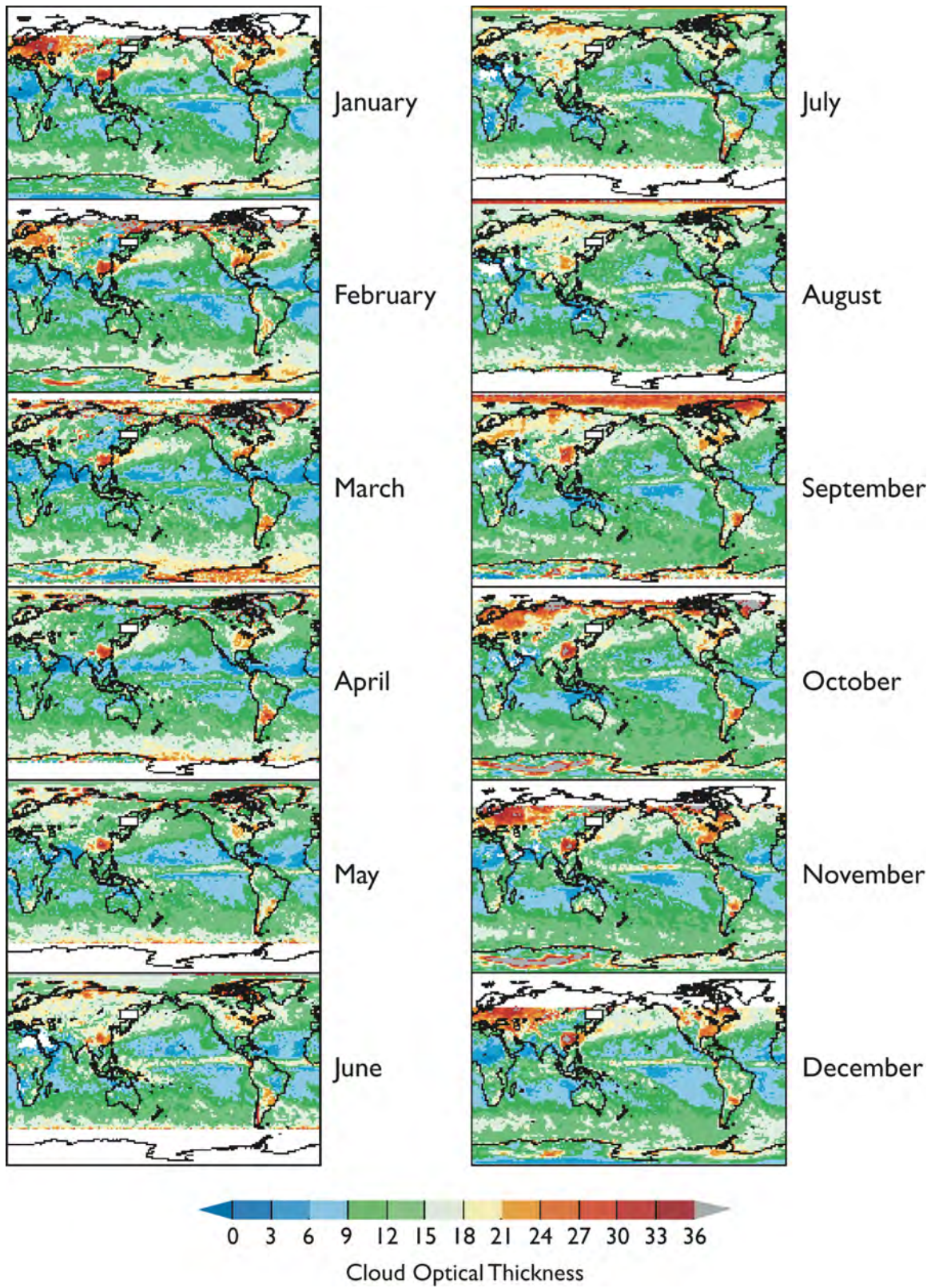


Figure 1. Monthly mean cloud optical thickness from April 2000-July 2003.

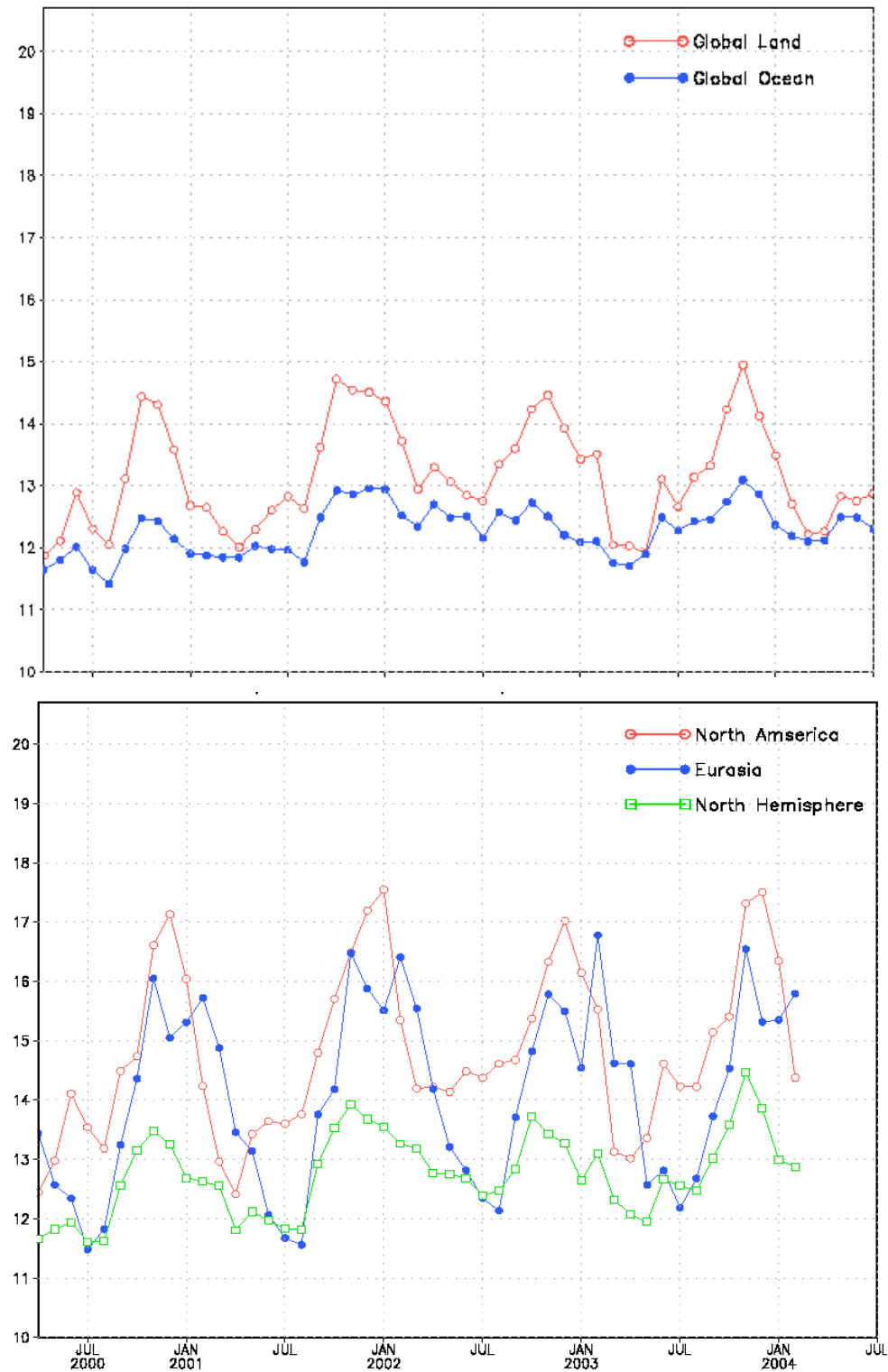
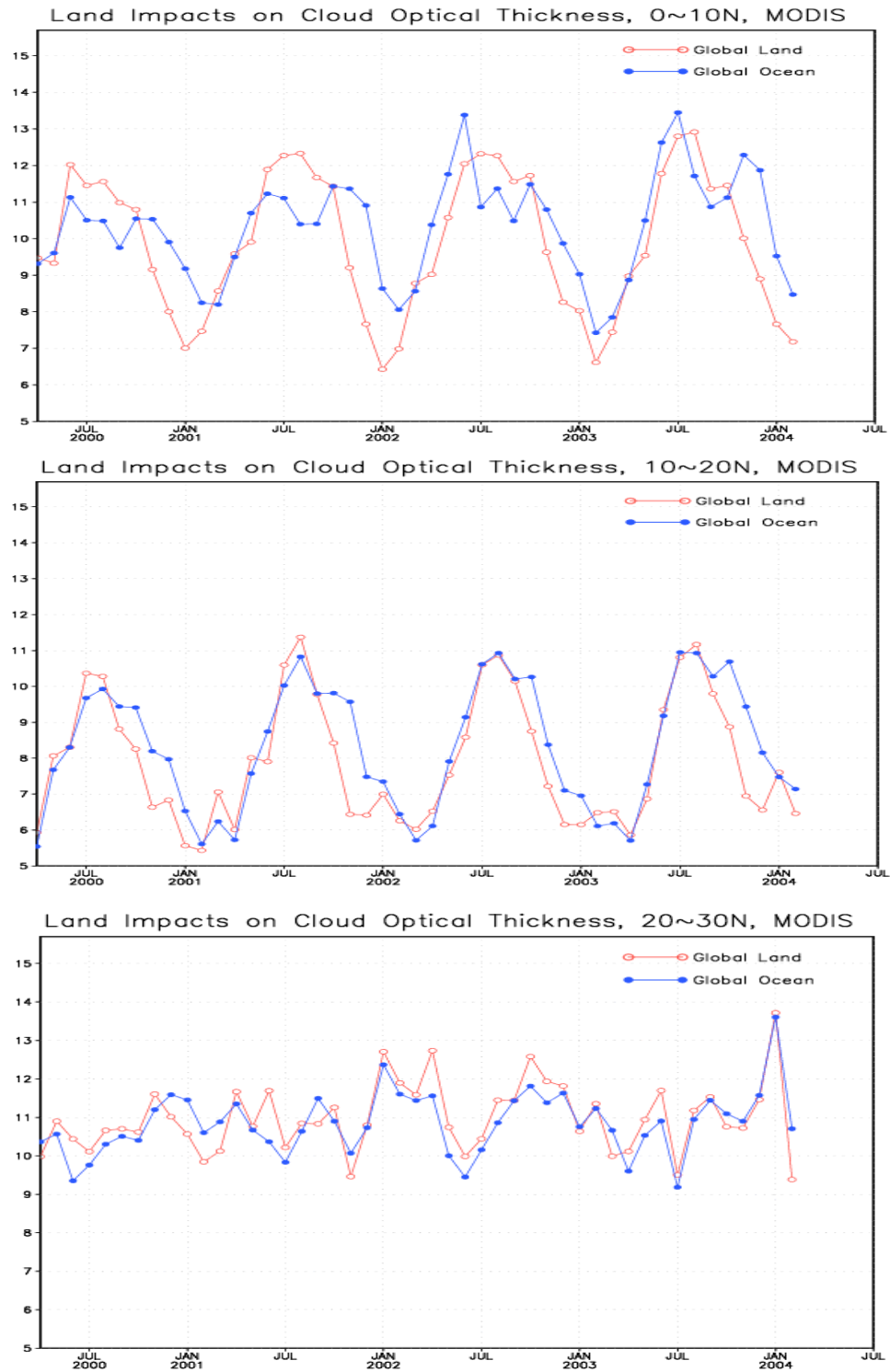


Figure 2. Monthly mean cloud optical thickness as a function of time (a) for global land and ocean, and (b) for North America, Eurasia, and the Northern Hemisphere.



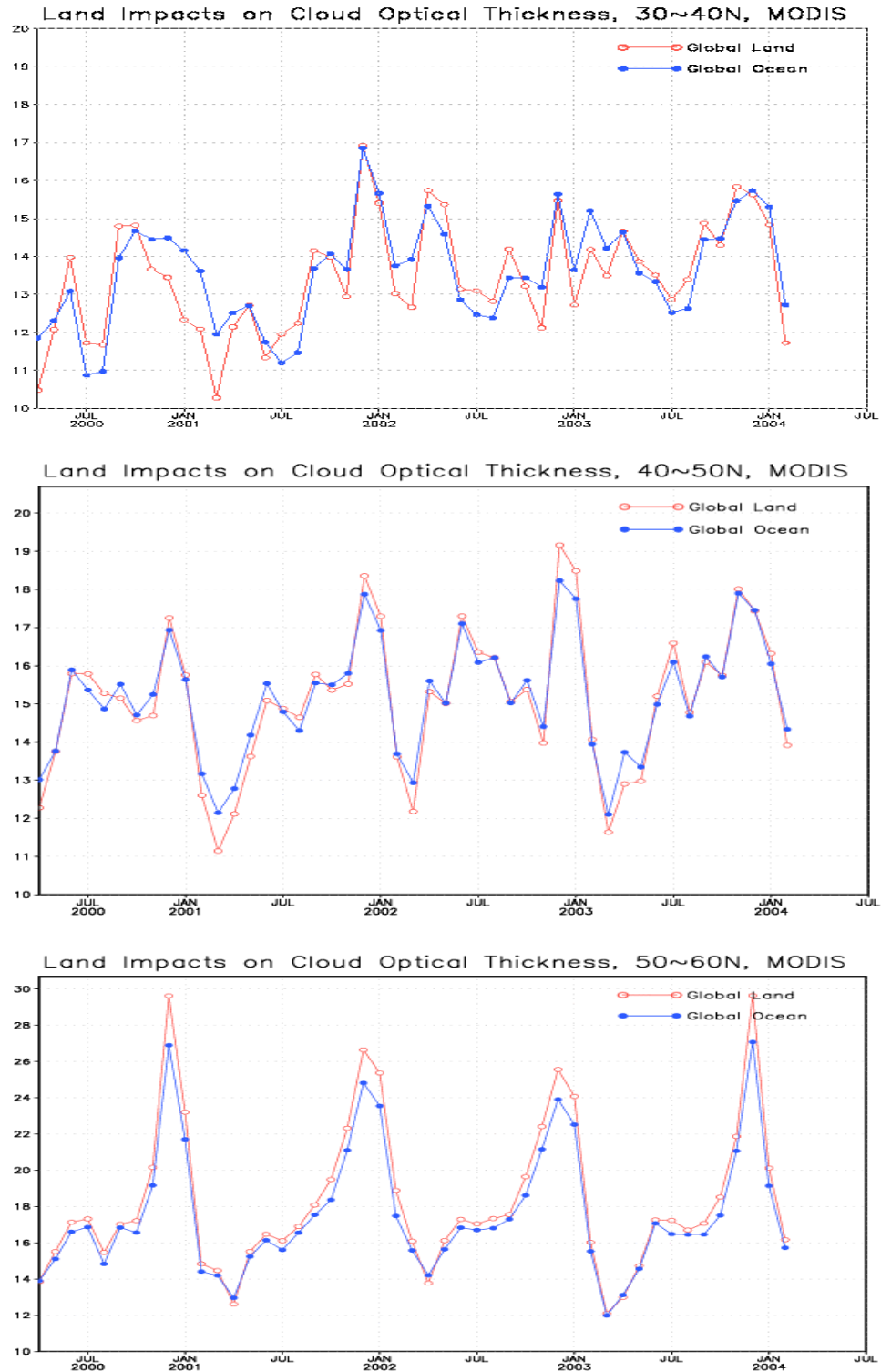
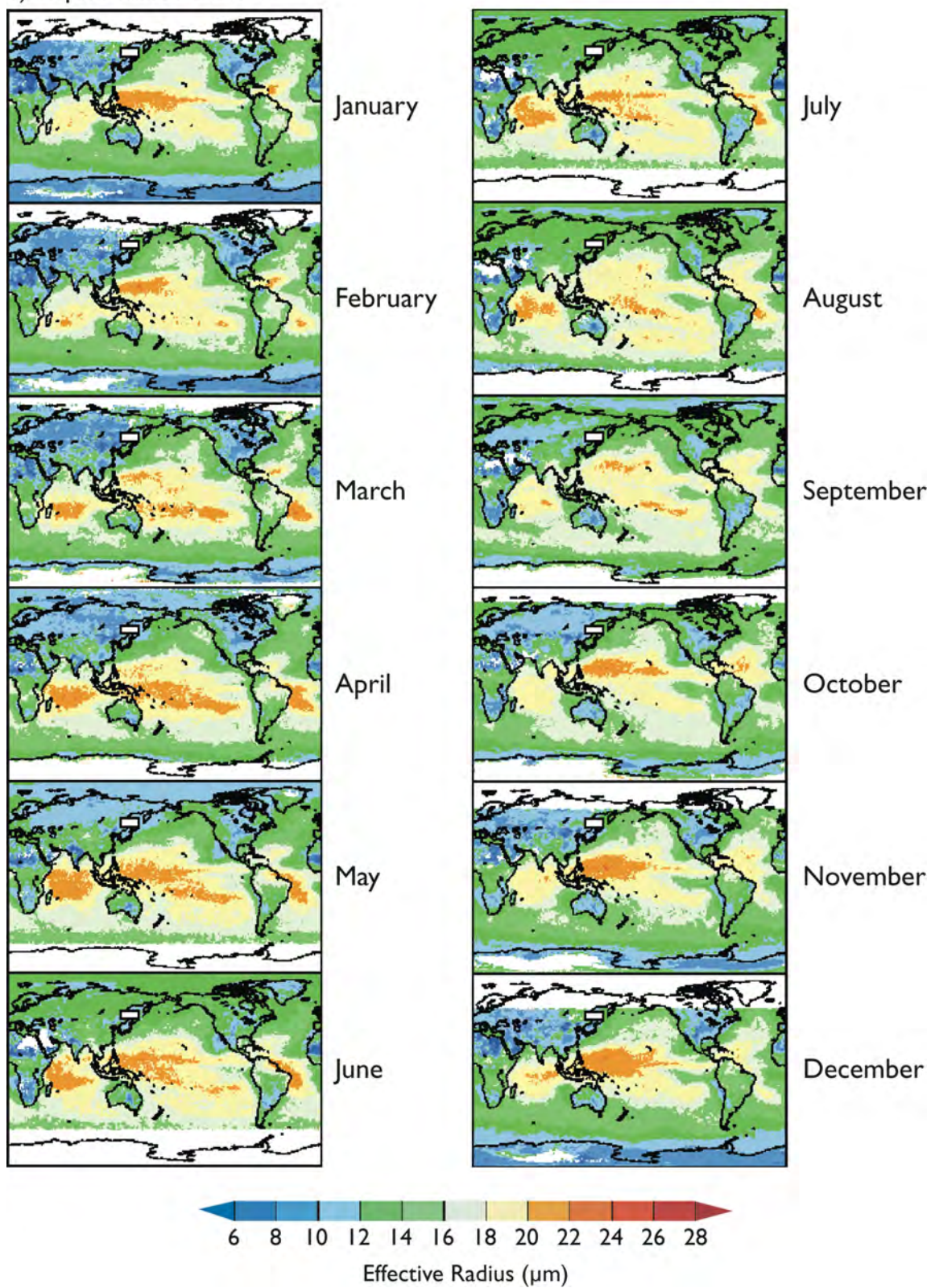


Figure 3. Zonal mean cloud optical thickness as a function of time for land and ocean regimes. In the legend, “Global Land” and “Global Ocean” means zonal averages for land and ocean for the specific latitude bands, respectively.



## a) Liquid Water Clouds





## b) Ice Clouds

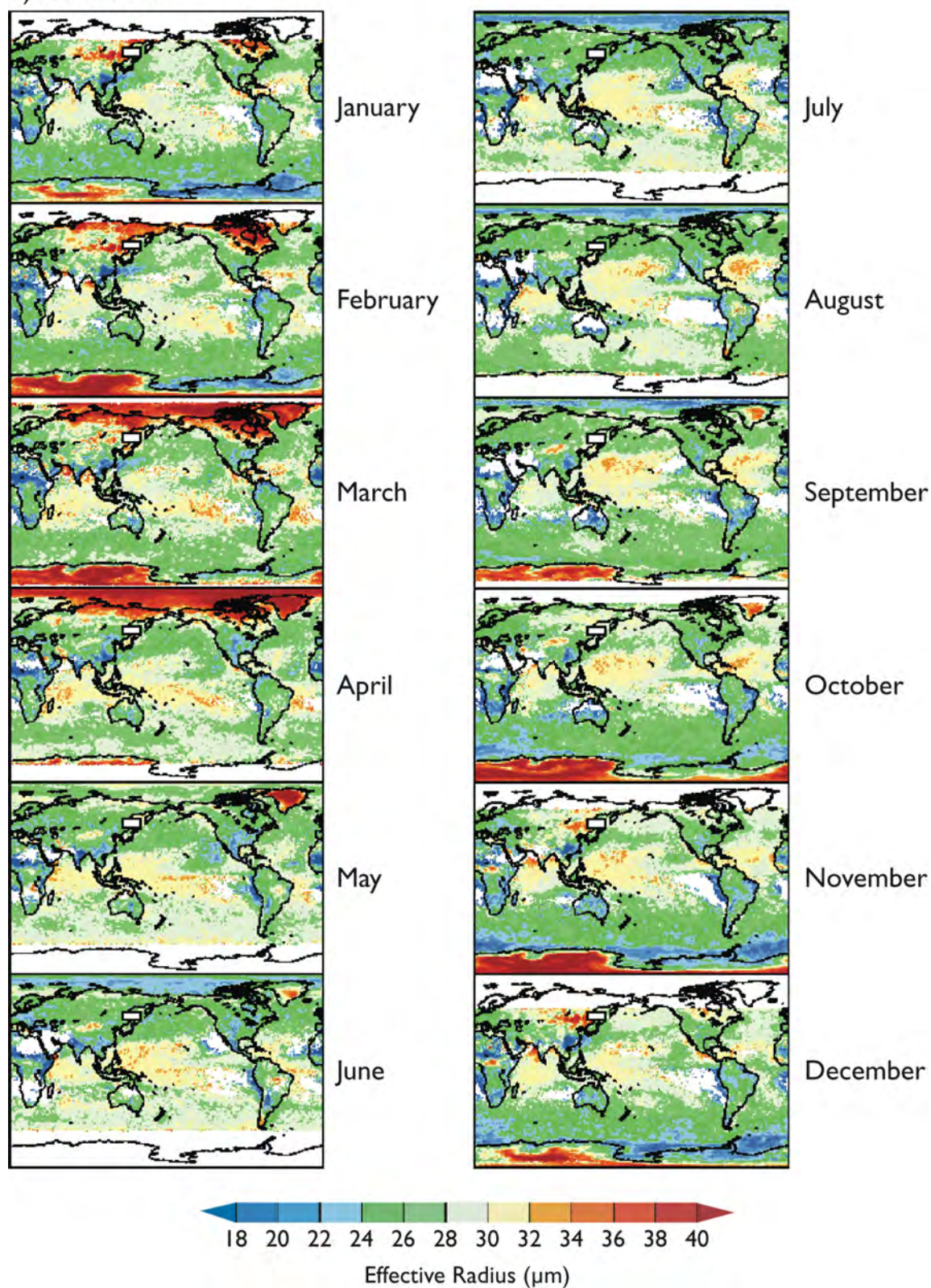
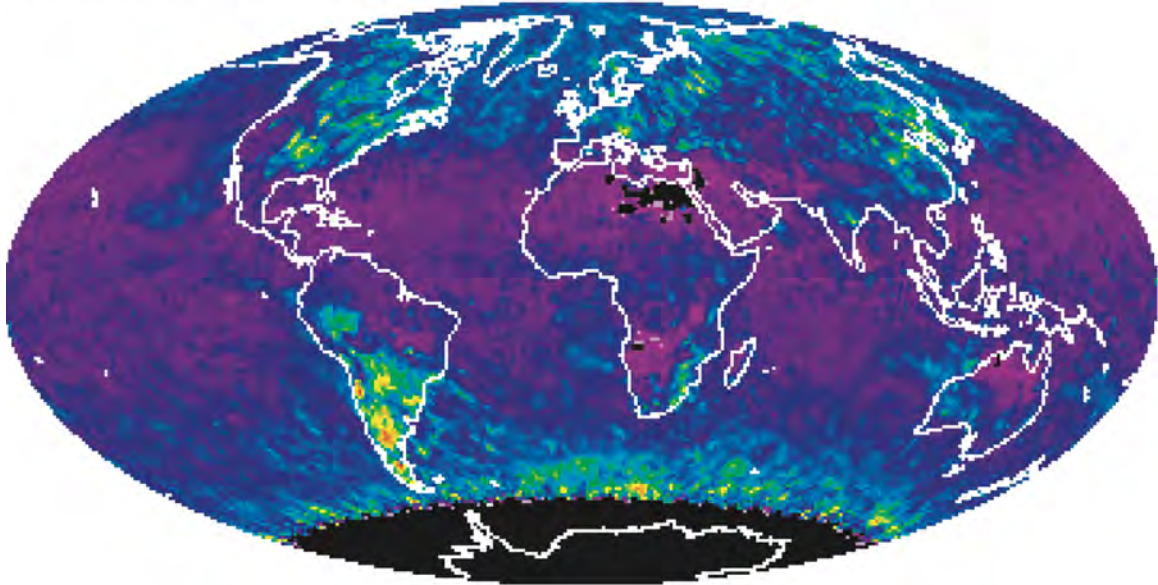


Figure 4. Monthly mean cloud effective radius for (a) liquid water clouds and (b) ice clouds from April 2000-July 2003.



a) Cloud Optical Thickness Standard Deviation (Liquid Water)



a) Cloud Optical Thickness Standard Deviation (Ice)

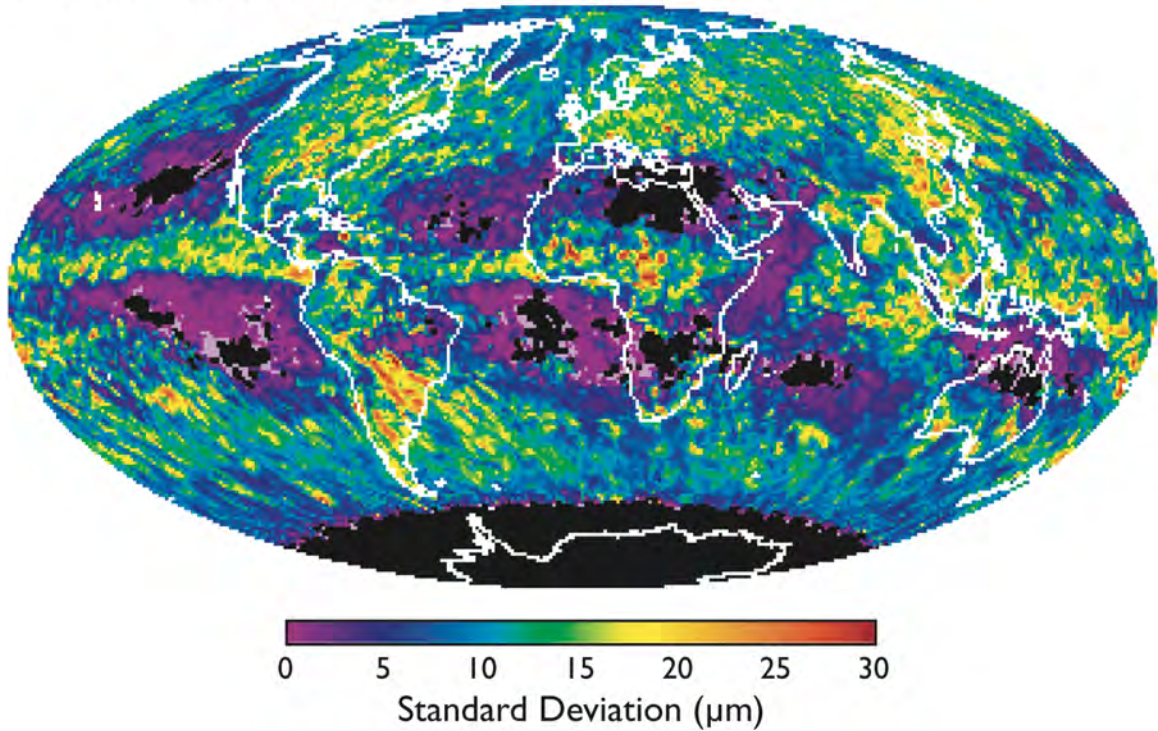


Figure 5. Monthly mean standard deviation of cloud optical thickness for  $1^\circ \times 1^\circ$  grid cells on July 2004 for (a) liquid water clouds and (b) ice clouds.

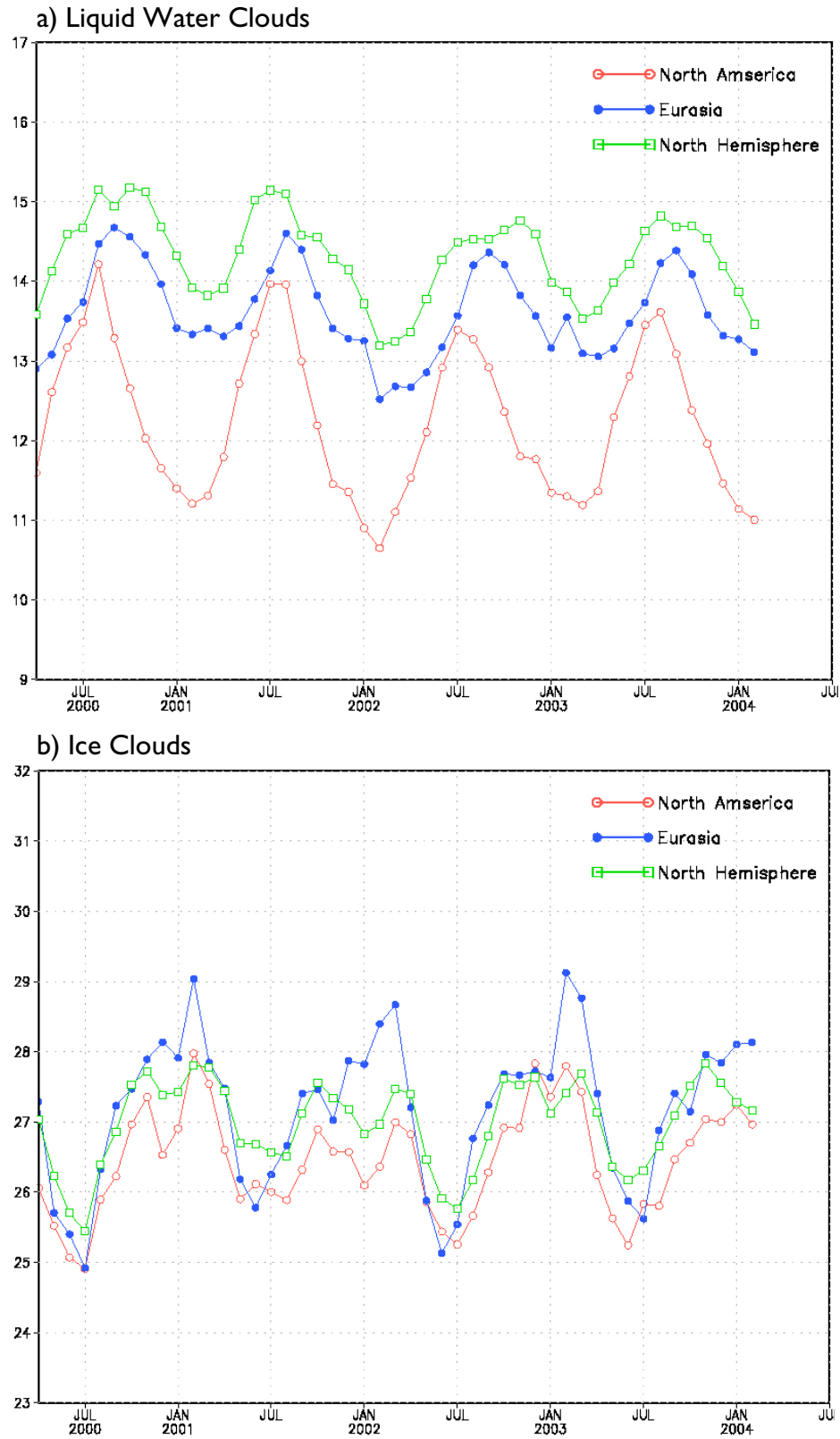


Figure 6. Monthly mean cloud effective radius as a function of time for (a) liquid water clouds and (b) ice clouds.



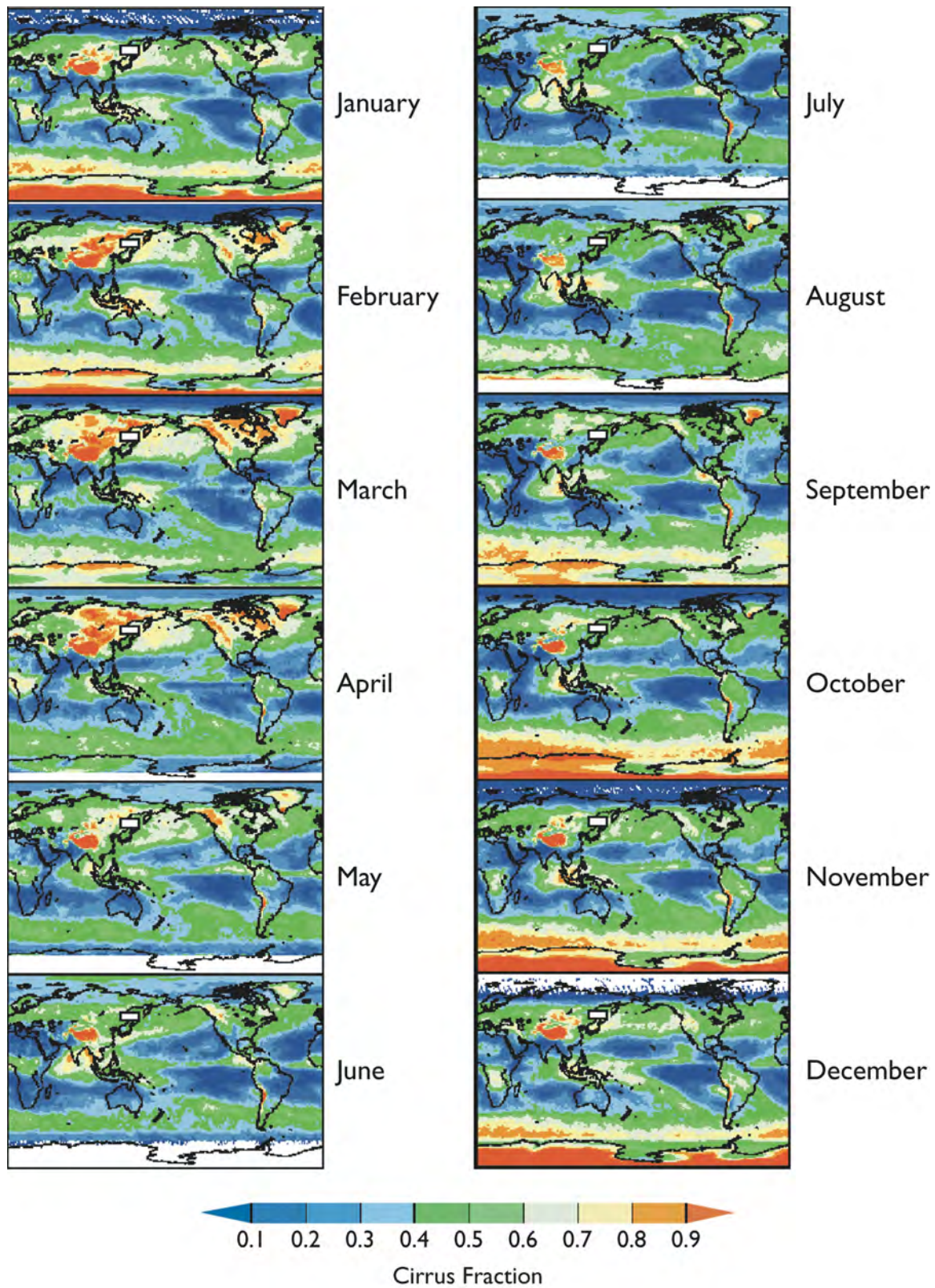


Figure 7. Monthly mean cirrus fraction from April 2000-July 2003.

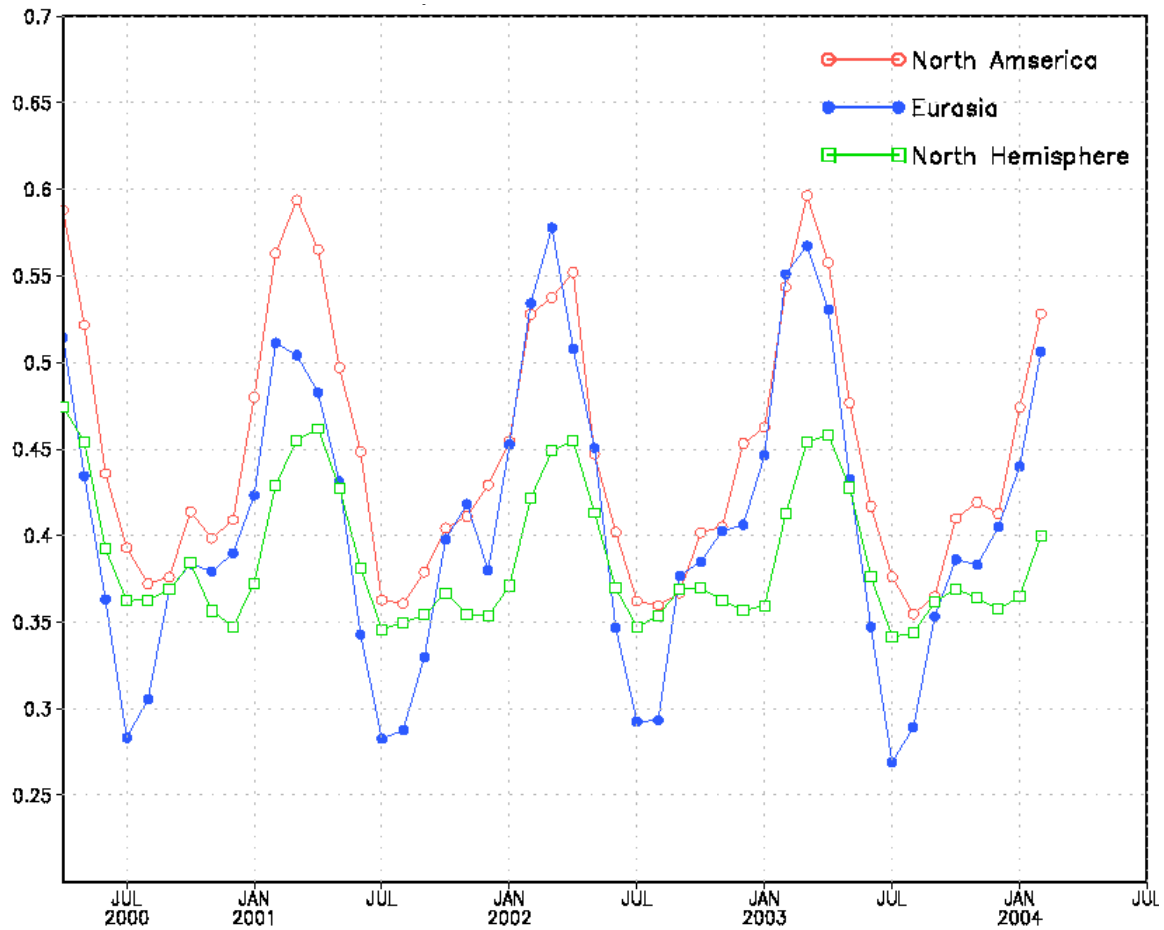
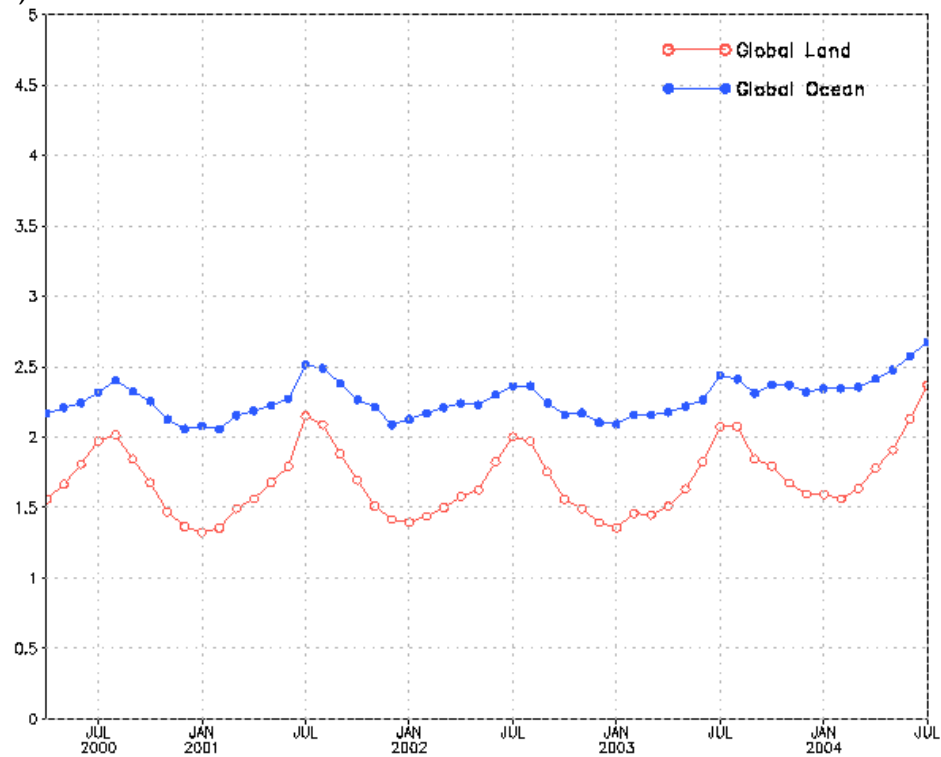


Figure 8. Monthly mean cirrus fraction as a function of time for North America, Eurasia, and the Northern Hemisphere.

a) Global Land and Ocean



b) Land Regions and the Northern Hemisphere Ocean

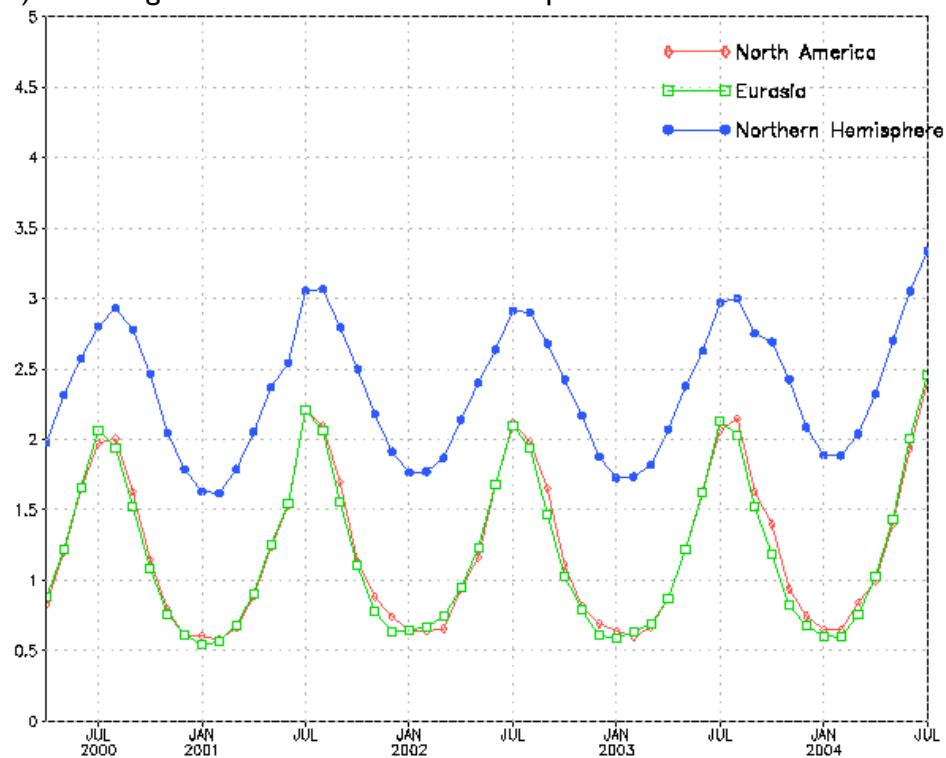
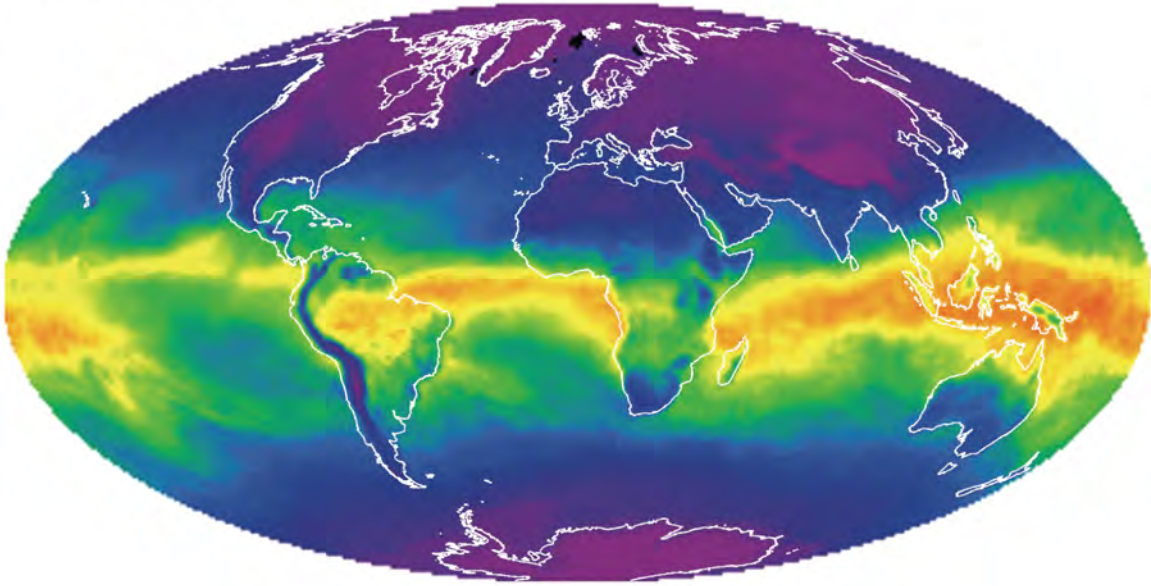


Figure 9: Monthly mean precipitable water as a function of time (a) for global land and ocean, and (b) for North America, Eurasia, and the Northern Hemisphere ocean.



a) January 2004



b) July 2004

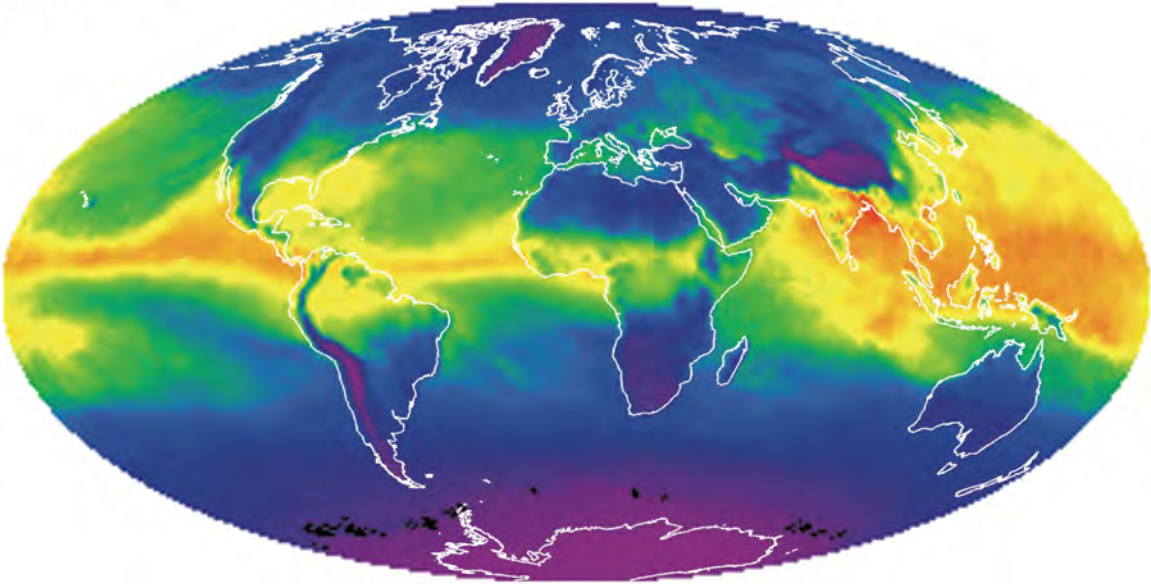


Figure 10: Monthly mean precipitable water for (a) July 2004 and (b) January 2004.

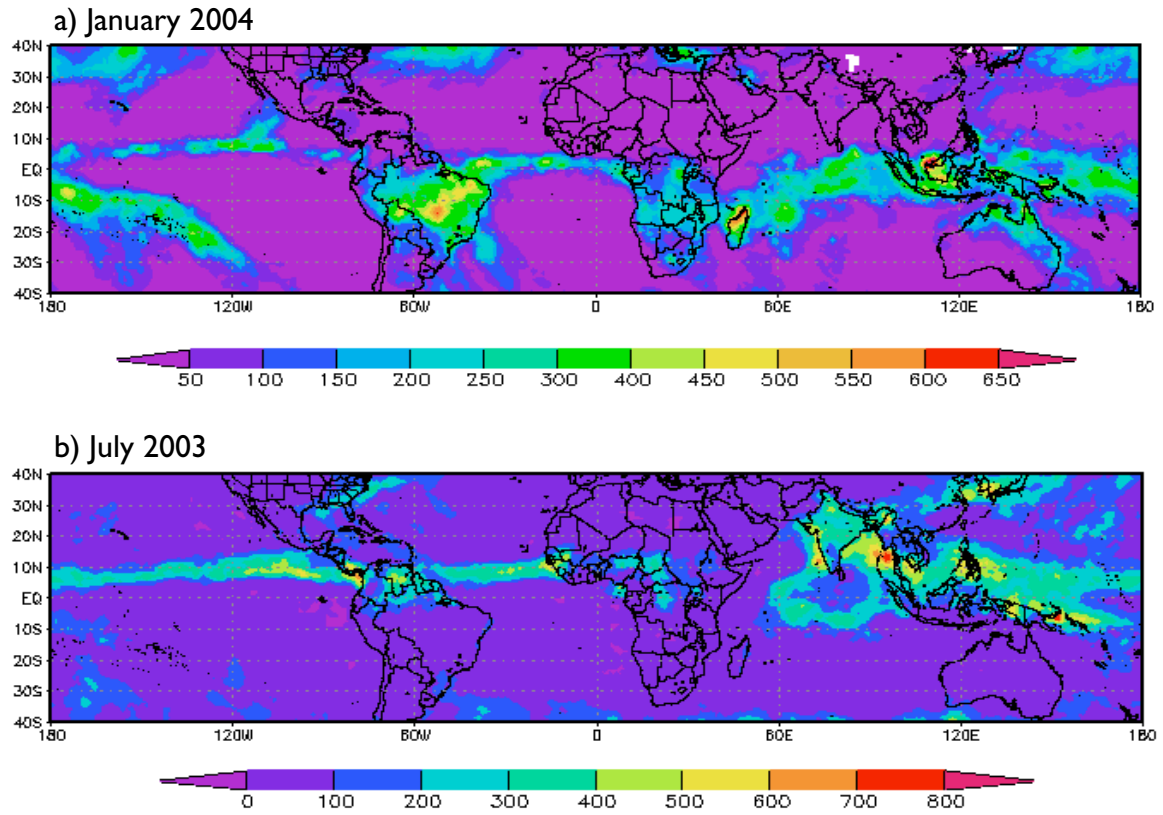


Figure 11. Accumulated rainfall measured from TRMM for (a) January 2004 and (b) July 2003.



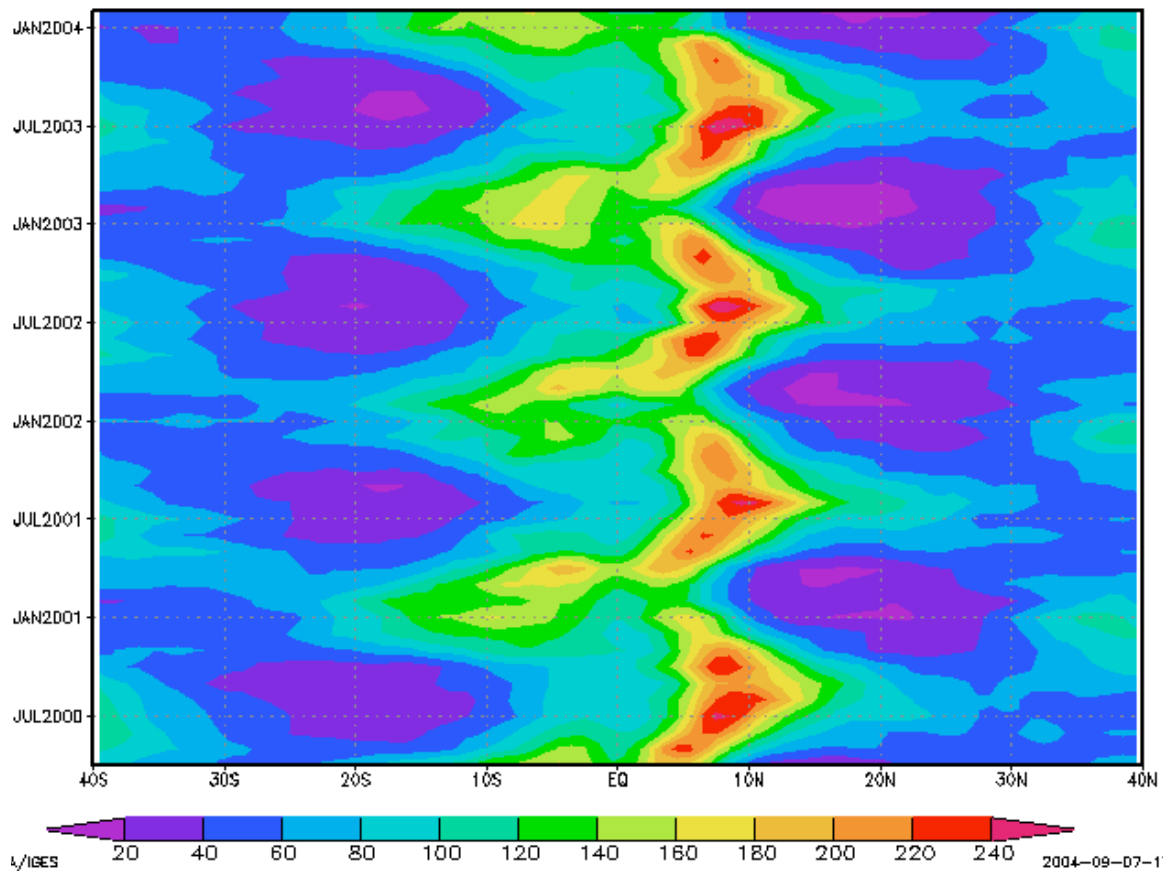


Figure 12. Zonally-averaged monthly mean accumulated rainfall from TRMM observations at 180°W.

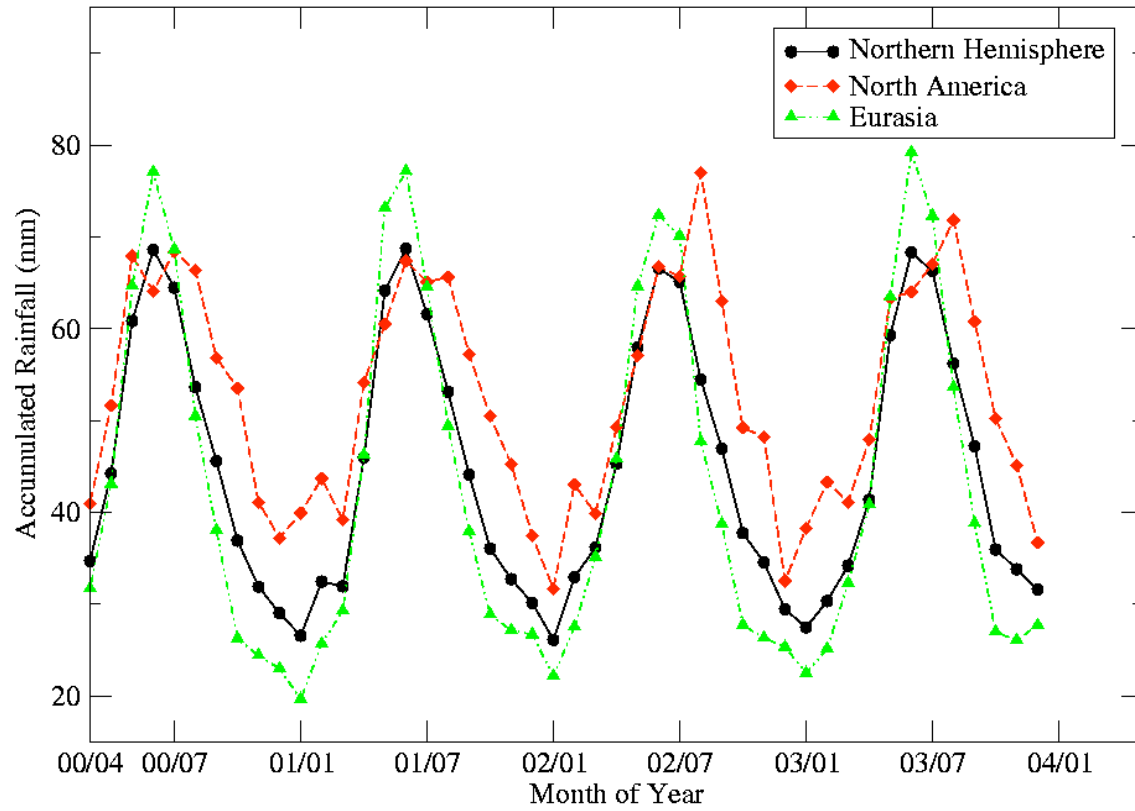


Figure 13. Monthly rainfall for the Northern Hemisphere, North America, and Eurasia. Data are based on GPCP analysis.

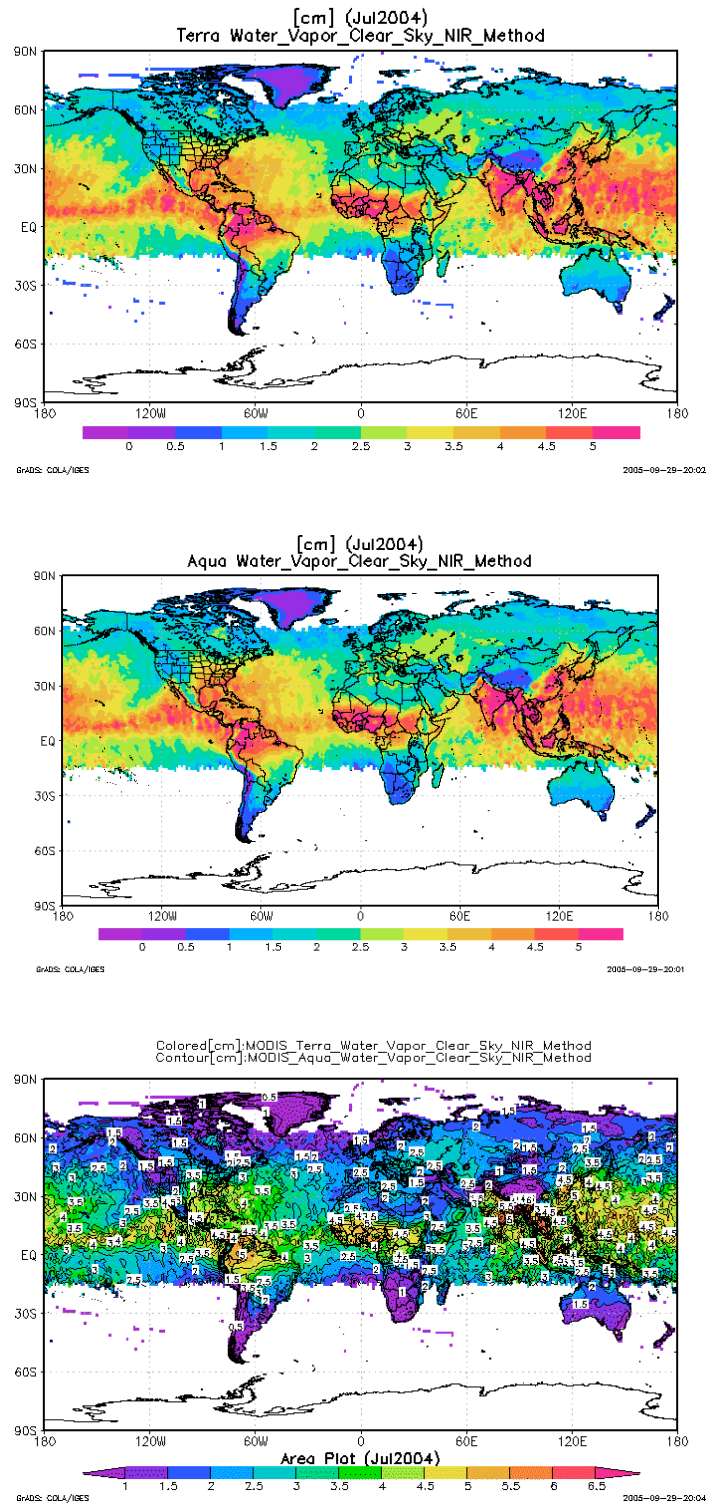


Figure 14: Diurnal signal of water vapor over land vs. ocean. (a) Terra water vapor observations for July 2004; (b) same as (a) except for Aqua; and (c) the difference between afternoon and morning Aqua minus Terra). Note that the data southward of 15°S is un-retrieval in

MODIS water vapor NIR algorithm (Gao et al. 2002).

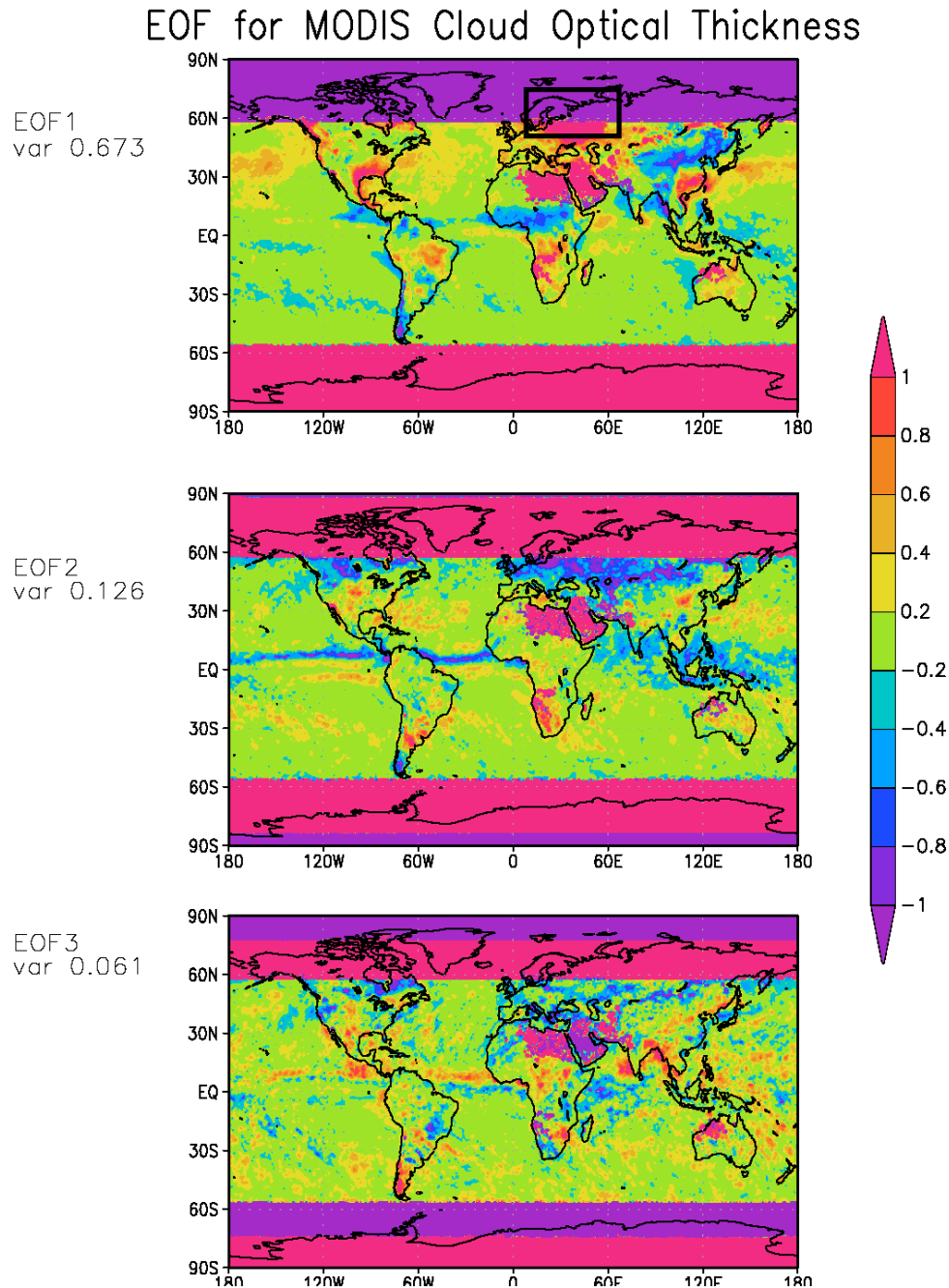


Figure 15. EOF reanalysis on 5-year (April 2000 – April 2005) monthly Terra/MODIS measurement for cloud optical thickness. (a) is the first principal component (EOF1); (b) is the second principal component (EOF2); and (c) is the third principal component (EOF3). The explained variance for each component is given at the left of each panel. The extremely small values poleward of 60°N and 60°S and the box-outlined regions over Africa are missing values.

## EOF for MODIS Cloud Optical Thickness, summer

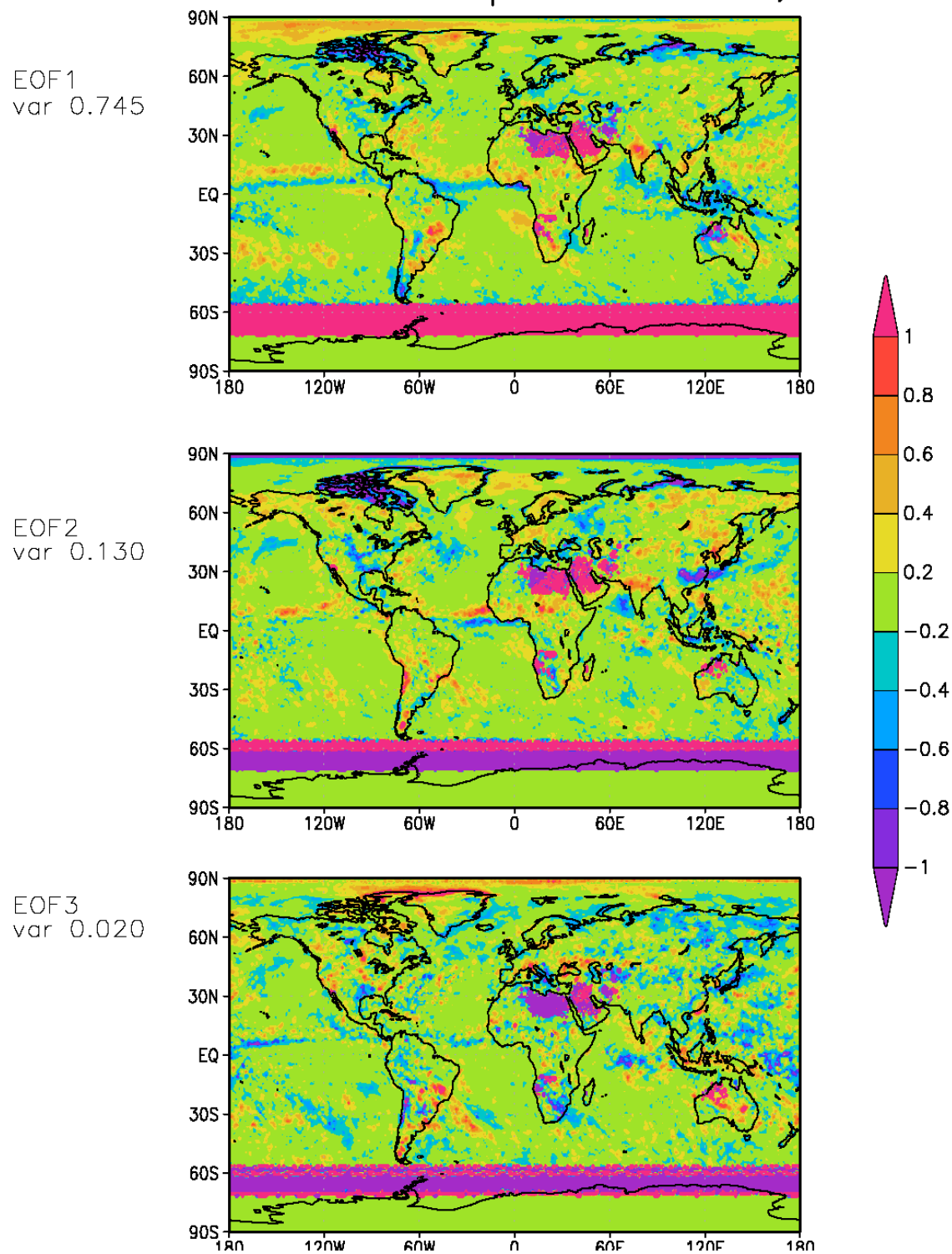


Figure 16. As in Figure 15, except for summer clouds.



## EOF for MODIS Atmospheric Water Vapor, summer

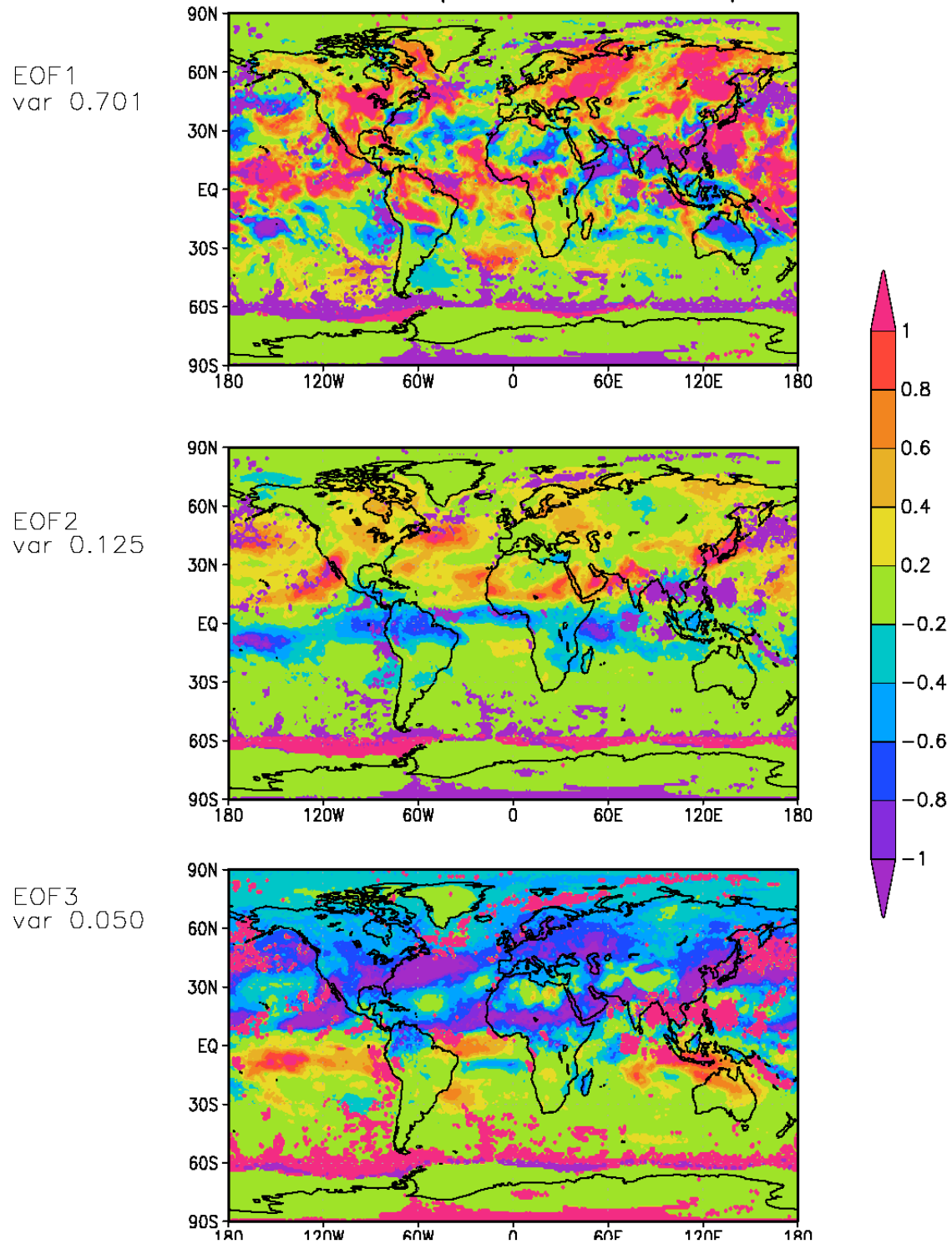


Figure 17. Results of EOF analysis on 5-year MODIS water vapor for summer time. (a) is EOF1; (b) is EOF2, and (c) EOF3.

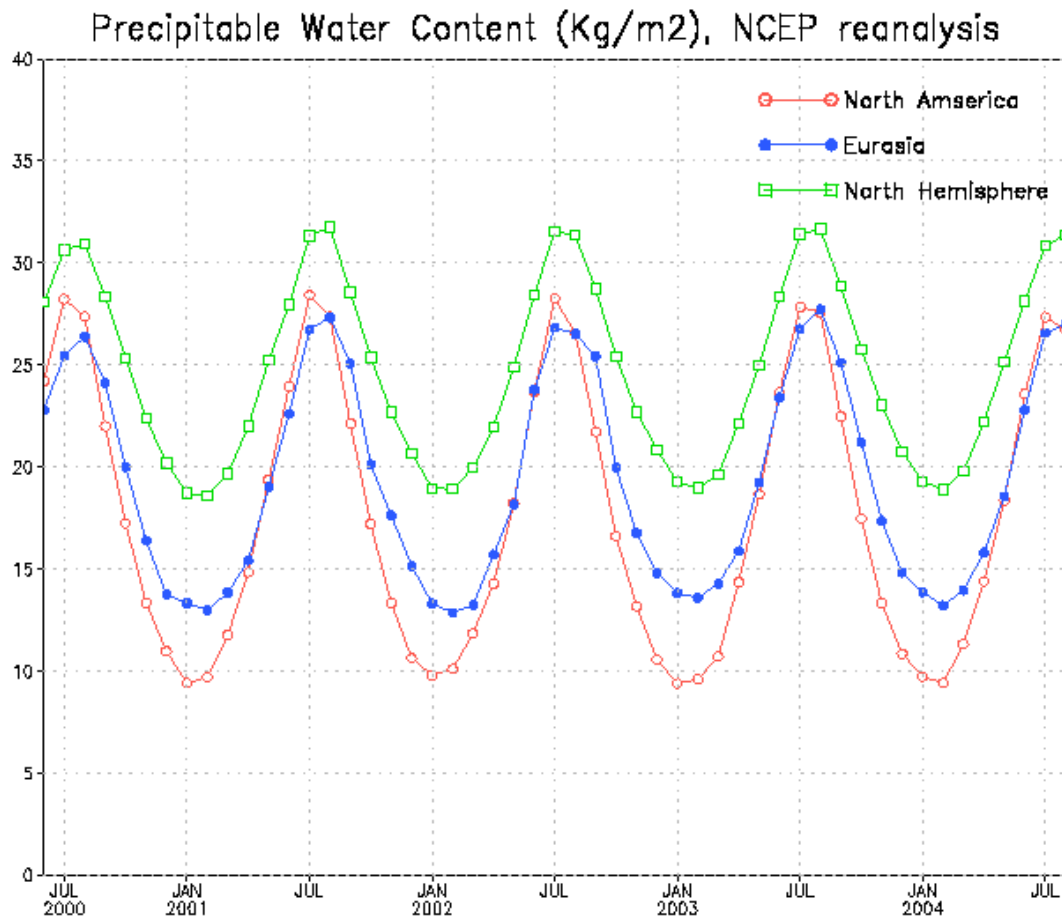


Figure 18. NCEP reanalysis simulated precipitable water vapor for North America, Eurasia, and the North Hemisphere.